Journal of Materials Chemistry A

ROYAL SOCIETY OF CHEMISTRY

PAPER

View Article Online
View Journal | View Issue

Cite this: J. Mater. Chem. A, 2024, 12, 29708

Non-thermal plasma enabled catalytic dry reforming of methane over a ceria nanorod supported NiO catalyst: the role of Ru as a coke resistant active site†

Md Robayet Ahasan,[a] Md Monir Hossain[b] and Ruigang Wang *[b]

This study reports that a 14 wt% Ni–1 wt% Ru bimetallic catalyst supported on ceria (CeO_2) nanorods (NRs) synthesized *via* wet impregnation can offer superior conversion and stability against coking during non-thermal plasma (NTP)-assisted dry reforming of methane (DRM) compared to monometallic Ni or Ru catalysts. This study revealed that when Ru was introduced as a promoter into the CeO_2 NR supported Ni catalyst, the DRM conversion percentage increased significantly under NTP (CH_4: 92% and CO_2: 70%) at 450 °C. Unlike thermal catalysis, plasma catalysis resulted in high yield (46% CO and 40% H_2) and selectivity (62% CO and 42% H_2) at 450 °C. Additionally, the durability (60 minutes) of the catalyst was tested at 350 °C. The bimetallic synergy and formation of CeO_2 NR supported Ni–O–Ru solid solution are believed to be the main causes of the significantly improved CH_4 and CO_2 conversions. The high coking resistance of the CeO_2-NR supported Ni–Ru bimetallic catalyst is attributed to three major factors: (1) the role of Ru in weakening the bond between Ni sites and carbon; (2) the higher dispersion of Ni over the CeO_2 NR surface; and (3) the accessibility of surface and lattice oxygen over the CeO_2 NR support, which promotes excellent redox properties and carbon oxidation. The proposed non-equilibrium and bimetallic synergy approach paves the way for cost-efficient and durable DRM catalysts for scalable syngas production from two potent greenhouse gases, which could potentially apply to future energy-efficient industrial processes such as the production of syngas and other value-added chemicals.

Received 15th June 2024
Accepted 19th September 2024

DOI: 10.1039/d4ta04141k

rsc.li/materials-a

1. Introduction

The depletion and environmental concerns associated with the consumption of fossil fuel resources have driven the energy industry to search for alternative strategies. Because of the abundance and accessibility of feedstocks, dry reforming of methane (DRM) is a readily scalable gas reforming technology for refining two primary greenhouse gases (GHGs), namely, carbon dioxide (CO_2) and methane (CH_4), to syngas (a mixture of CO and H_2) (eqn (1)). Syngas is a vital chemical energy source for the Fischer–Tropsch synthesis of value-added fuels and chemicals.[1,2]

$$CH_4(g) + CO_2(g) \rightleftharpoons 2CO(g) + 2H_2(g) \quad (1)$$

Nevertheless, DRM is an endothermic procedure that requires excess thermal energy (>700 °C).[3] The spontaneous reaction is thermodynamically impossible at low temperatures considering that negative Gibbs free energy is not fulfilled. Non-thermal plasma (NTP) or cold plasma technology offers a viable alternative to the traditional catalytic approach for DRM conversion owing to its non-thermal and non-equilibrium properties, lower energy demand, and unique ability to trigger chemical and physical reactions at relatively low temperatures. In NTP, the average kinetic temperature of the gas stays low. In contrast, energetic electrons with a typical electron temperature of 10 000–100 000 K (1–10 eV) can split inert CO_2 and CH_4 molecules to generate extremely activated species such as ionized particles, molecules, and free radicals. Hence, electron temperature rather than thermal processes drives chemical reactions under NTP.[4–6] Eqn (2)–(4) present a few examples of easy NTP integrated electron impact dissociation of CH_4 and CO_2, which require relatively high temperatures for conventional thermal dissociation.

$$CH_4 + e^- \rightleftharpoons CH_3^* + H^* + e^- \quad (2)$$

$$CH_4 + e^- \rightleftharpoons CH_2^* + H_2 + e^- \quad (3)$$

$$CO_2 + e^- \rightleftharpoons CO + O^* + e^- \quad (4)$$

[a]Department of Metallurgical and Materials Engineering, The University of Alabama, Tuscaloosa, AL 35487, USA
[b]Department of Chemical Engineering and Materials Science, Michigan State University, East Lansing, MI 48824, USA. E-mail: rwang@msu.edu

† Electronic supplementary information (ESI) available. See DOI: https://doi.org/10.1039/d4ta04141k

Since CH_4 and CO_2 have relatively stable chemical structures and dry reforming feedstocks typically have a higher carbon deposition, obtaining a high selectivity and yield from CH_4 and CO_2 reforming requires specialized or complicated techniques. Thus, various catalysts or supported catalysts have been utilized to activate the C–H and C–O bonds in stable CH_4 and CO_2 reactants. Prior research has demonstrated that although the catalyst sources for DRM can be group VIII metals from the periodic table, *i.e.*, Ru, Rh, Pt, Co, and Ni, from a commercial perspective, Ni is the most suitable or sustainable catalyst material especially because it is affordable and easily accessible.[7,8] However, the catalyst deactivation induced by the potential deposition of coke on catalysts is the primary barrier to its industrial application at the present time. According to scientific literature, the coking issue can be addressed using promoters like noble metals including Ru and Pt, which promote the activation of H_2 from CH_4 dissociation or dehydrogenation (H_2 spillover effect) and enhance the NiO reduction at lower temperature.[9,10] Besides, it has been reported that bimetallic catalysts can outperform their monometallic counterparts in terms of conversion, yield, selectivity, and coke resistance.[11–13] For instance, Duan *et al.*[14] reported reduced carbon deposition for Mg(Al)O supported bimetallic Ni_9Co_3 (31 wt%) and Ni_6Co_6 (21 wt%) catalysts in DRM reaction, which is much better than monometallic Ni_9 (66 wt%) and Ni_6 (40 wt%) with a similar Ni content and support material. Similarly, Zafarnak *et al.*[15] observed that bimetallic catalysts exceeded monometallic catalysts in terms of DRM activity under the same reaction conditions, indicating a potential synergistic effect of two different metals. According to their report, 10 wt% Ni–10 wt% Co/mullite converted 87% CH_4 and 85% CO_2 at 750 °C, while 20% Ni/mullite and 20% Co/mullite had a CH_4 and CO_2 conversion below 80%. Although several catalytic DRM experiments are available in the literature, most of these are conventional thermal catalytic DRM. However, this research remarkably blends the advantages of NTP and bimetallic synergy of Ni and Ru catalysts on a surface-engineered CeO_2 NR support, which established significant improvements of low-temperature conversion compared to conventional thermal DRM.

In this study, CeO_2 NR supported 14 wt% Ni and 1 wt% Ru catalysts were synthesized by a wet impregnation method and assessed for DRM under thermal and non-thermal plasma environments. The correlation between catalytic activity and catalyst properties was investigated using XRD, Raman, TPR, TPD, XPS, and TEM techniques.

2. Materials and methods

2.1 Catalyst synthesis

2.1.1 Chemicals. Cerium(III) nitrate hexahydrate ($Ce(NO_3)_3 \cdot 6H_2O$, 99.5% pure) was bought from Acros Organics. Both sodium hydroxide (NaOH, 99% pure) and ammonium hydroxide ($NH_3 \cdot H_2O$, BDH, 28–30 vol%) were acquired from VWR. The catalyst precurors were ruthenium nitrosyl trinitrate [$Ru(NO)(NO_3)_3$] and nickel(II) nitrate hexahydrate [$Ni(NO_3)_2 \cdot 6H_2O$] from Alfa Aesar, both of which were 99.9% pure. The compounds were utilized without any additional processing.

2.1.2 Preparation of the CeO_2 NR support. To prepare 88 mL of 0.1 M $Ce(NO_3)_3 \cdot 6H_2O$ solution, 3.8403 g of $Ce(NO_3)_3 \cdot 6H_2O$ was added to 88 mL of DI (deionized) water.[16–18] Simultaneously, 1.93 g of NaOH was dissolved in 8 mL of DI water to prepare an aqueous solution of 6 M NaOH. Then, the 8 mL solution of NaOH (6.0 M) was mixed drop by drop with the 88 mL solution of $Ce(NO_3)_3 \cdot 6H_2O$ (0.1 M) and stirred vigorously in a 200 mL Teflon autoclave liner. The solution was mixed for 15 seconds prior to transferring the Teflon liner to an autoclave made of stainless steel and sealing it carefully. The autoclave was kept in an oven for 48 hours at 90 °C. The autoclave was subsequently lowered to ambient temperature, and the precipitate was thoroughly washed with approximately 500 mL of DI water to eliminate any leftover NO_3 and Na^+ ions. The CeO_2 NR were cleaned with 50 mL of ethanol to prevent hard aggregation and baked for 12 hours at 60 °C. The support was then collected and crushed with a mortar and pestle.

2.1.3 Preparation of Ni–Ru/CeO_2 NR bimetallic catalysts. Ru and Ni were loaded on the CeO_2 NR support *via* wet impregnation with aqueous $Ru(NO)(NO_3)_3$ and $Ni(NO_3)_2 \cdot 6H_2O$ solutions. In 200 mL beakers, 100 mL of deionized water was combined with 0.85 g of CeO_2 NR powder. Under vigorous stirring, 1 wt% Ru equivalent of $Ru(NO)(NO_3)_3$ and 14 wt% Ni equivalent of $Ni(NO_3)_2 \cdot 6H_2O$ precursors were added to the CeO_2 NR support powder suspension. The suspension solution was thoroughly mixed by magnetic stirring, and then a solution of $NH_3 \cdot H_2O$ (0.5 M, ammonium hydroxide, BDH, 28–30 vol%) was added slowly to maintain the pH value at ~9. The precipitate was heated at 80 °C for 4 hours while being stirred at 400 rpm. Afterward, the precipitate was placed in a drying oven for 24 hours at 80 °C. The sample was collected and crushed using a mortar and pestle into a fine powder, and then calcined in a furnace for 5 hours at 350 °C with a ramp of 10 °C min^{-1}.

2.2 Catalyst characterization

Powder X-ray diffraction (XRD) was used to examine the crystal structures of the produced catalysts employing a Phillips X'Pert MPD diffractometer set to a voltage of 40 kV and a current of 40 mA with a copper Kα radiation source ($\lambda = 0.154$ nm). Each profile was scanned at 0.5° min^{-1} with a range of 2θ between 10° and 90°. Jade software was used to examine the lattice properties and average crystal size of each catalyst using the acquired XRD patterns.

The nitrogen adsorption–desorption isotherm at 77 K was used to calculate the Brunauer–Emmett–Teller (BET) surface area using a Micromeritics AutoChem II 2920 chemisorption analyzer. Hydrogen temperature-programmed reduction (H_2-TPR) and carbon dioxide temperature-programmed desorption (CO_2-TPD) were both characterized using the same apparatus. For the H_2-TPR study, 85–95 mg of each powder sample was put in a quartz U-tube sandwiched between two pieces of quartz wool and heated at 10 °C min^{-1} from 30 °C to 900 °C. The samples were then reduced in a combination of 10% H_2

and 90% Ar while maintaining a 50 mL min^{-1} flow rate. A calibrated thermal conductivity detector (TCD) was used to detect the H_2 signal, and the amount of H_2 consumed during the reduction was determined (calibrated) by a quantitative reduction of CuO to metallic copper. For the CO_2-TPD analysis, the sample was placed in a quartz U-tube with a helium (He) stream (flow rate: 50 mL min^{-1}) and heated from room temperature to 400 °C to eliminate any remaining moisture. Following a 60 minute cool-down period to ambient temperature, the sample was subjected to a gas combination of 10% CO_2 and 90% He at a 50 mL min^{-1} flow rate. Under He gas, the sample was heated linearly until 900 °C at a flow rate of 10 °C min^{-1}. At increased temperatures, the CO_2 desorption behavior was evaluated using a TCD.

A transmission electron microscope (TEM, Model: FEI Tecnai F20, 200 kV acceleration voltage) was used to collect high-resolution transmission electron microscopy (HRTEM) images to investigate the particle morphology/size and microstructures. Powder agglomeration and elemental distribution were determined utilizing a JEOL 7000 FE SEM with an energy dispersive X-ray spectrometer (EDX). The powder samples were ultrasonically dispersed in ethanol for TEM sample preparation. Before analysis, a tiny amount of suspension solution (typically one/two drops) was accumulated on an ultrathin carbon film affixed to a 400-mesh copper grid (Ted Pella Inc.) and dried for two hours.

X-ray photoelectron spectroscopy (XPS) analysis was done using a Kratos Axis Ultra DLD spectrometer equipped with a monochromatic Al Kα ($h\nu = 1486.6$ eV) source and ultra-high vacuum (10^{-10} Torr), and the surface chemical composition of the synthesized samples was determined from the obtained profile data. Carbon (C) 1s at 284.8 eV was used to calibrate the XPS binding energies (BE). Using CASA XPS software, the spectrum was fitted and deconvoluted.

A Raman spectrometer (Model: Horiba LabRAM HR 800, objective: 100×) was used to non-destructively characterize the catalysts' elemental coordination environment spanning the spectral range of 100 to 1200 cm^{-1}. A Si single-crystal wafer was used to calibrate the spectrometer prior to each study. Excitation was performed with a laser system (Model: Laser Quantum MPC6000, diode-pumped solid-state) calibrated to $\lambda = 532$ nm wavelength.

2.3 Reactor setup

The DRM activity was assessed by placing the catalysts in an atmospheric-pressure fixed-bed dielectric barrier discharge (DBD) reactor system.[19,20] The pictorial representation of the complete plasma reactor system is depicted in Fig. 1. The DBD reactor consists of four distinct modules: a gas distribution system, a core quartz reactor system, an experimental regulating section, and a flow gas assessment system. Three Brooks GF040 Multiflo thermal mass flow controllers (MFC) with <1 s response times, MFC-1, MFC-2, and MFC-3, are a part of the gas supply system. These MFCs regulate the CO_2, CH_4, and Ar streams with a purity of >99.99% from Airgas. The gas flow of

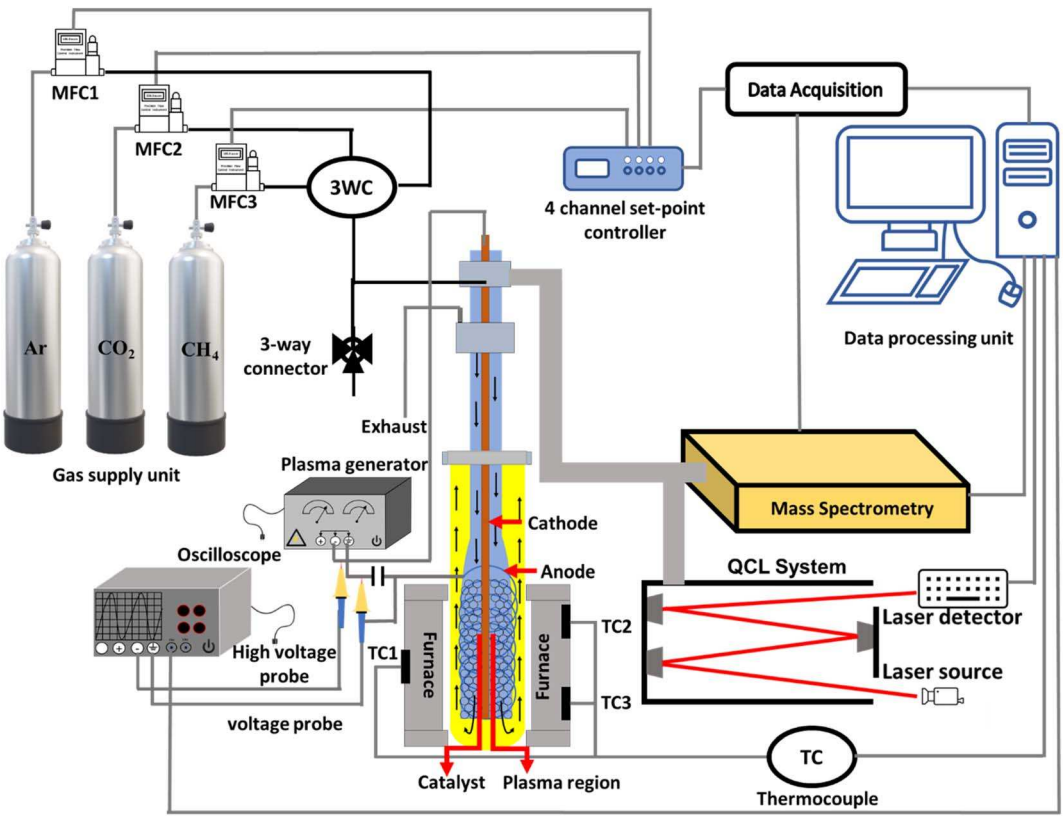

Fig. 1 Schematic of the atmospheric pressure DBD plasma reactor with accessories for DRM.

MFCs is controlled by a computer interface with a custom MATLAB GUI code through a national instrument (NI) card. The core quartz reactor system comprises two circular quartz tubes inside a furnace (Model: ATS 3210, Max temperature: 1200 °C). During operation, the temperature of the furnace is measured using thermocouples TC1, TC2, and TC3. The internal quartz tube (OD = 6.35 mm) is open-ended and has an expansion part (ID = 9.40 mm, length = 91.78 mm), while the outer quartz tube has a fixed diameter of 25.4 mm and a length of 91.78 mm. Two electrodes, with axial and wrapped shapes, are in the extended portion of the internal reactor tube. For plasma generation, the cathode (Kanthal A-1 wire, 24 g) is placed at the center axis of the tubes, and the anode (Kanthal A-1 wire, 32 g) is coiled around the inner tube's expansion portion. A dielectric barrier is created by covering the center electrode with a nonporous alumina ceramic tube (ID: 0.063 mm). The discharge gap of the electrodes is 6.12 mm. The supply gas system is connected through the internal quartz tube, allowing feed gases to enter first. The reactant gases first interact with the catalysts and plasma inside the inner tube before leaving *via* the open end. The catalyst sample was blended with quartz wool at the internal quartz tube's expansion section, where the plasma was created. The outer tube with a closed-end changes the gas direction so that it flows out to the exhaust. The exhaust gas mixture was studied utilizing a quadrupole mass spectrometer (QMS, model: MAX300-EGA) and a tunable diode quantum cascade laser absorption spectroscopy (TDLAS) system. The TDLAS system component consists of a quantum cascade laser (QCL) (Alpes Laser, sbcw6200 DN) with a controller as a laser supply, a homemade Herriott cell to improve gas absorption length, an IR detector to detect laser signal or intensity, an oscilloscope (Tektronix TBS1154, 150 MHz), and a waveform generator (B&K Precision, 4055B, 1 Hz to 60 MHz). The QMS collects gas samples from the end of the inner quartz through a small capillary quartz tube (OD: 0.80 mm, ID: 0.53 mm) and measures time-resolved concentration. The catalyst is placed in the plasma region at the expansion section of the inner tube. The TDLAS system collects samples from the exhaust line to detect C-2 products, like C_2H_6, C_2H_4, and C_2H_2, while the QMS system detects CO, H_2, CH_4, CO_2, and Ar. Before the operation, the TDLAS system's precision and the QMS's calibration were tested by flowing a known mixture of gases. A simultaneous stream of all gases (CH_4, CO_2, H_2, CO, O_2, and Ar) was required for calibration. A PVM500-2500 AC high-voltage power supply from Amazing1.com was connected to the DBD reactor to make uniform plasma. This power supply has a peak-to-peak voltage of 40 kV and a 20–70 kHz frequency. This study has a power supply frequency of 20 kHz. A high-voltage probe (Model: Tektronix P6015A) and a current transformer (Model: Magnelab, CT-E 0.5 BNC) were utilized to capture the electrical signals (applied voltage and current) in the oscilloscope that was connected to the TDLAS system. Each plasma-assisted DRM cycle comprises a 7 minute reduction cycle and a 3 minute purge with purified Ar gas. During the reduction, a total flow rate of 350 sccm and a ratio of 2.5 ($CO_2 : CH_4 = 250 : 100$ sccm) were maintained, while 100% Ar was streamed during the purge cycle to prepare the system for the following DRM cycle. The furnace regulates the reaction zone temperature, ranging between 150 and 450 °C at a rate of 4 °C min^{-1}.

2.4 Performance parameters

Conversion, yield, and selectivity are crucial parameters to evaluate the performance of any catalysis system. The conversion calculates the amount of reactant gas converted for every input unit. In a reaction, the selectivity measures the ratio of the desired product formed (in moles) to the portion of converted reactants. In contrast, the yield is the ratio of the desired product formed to the entire amount that is produced (100% yields indicate the absence of side reaction). The following formulas describe the feed gas conversion, product yield, and selectivity of the DRM reaction:

$$C_{CO_2} = \frac{\text{converted } CO_2 \text{ in moles}}{CO_2 \text{ input in moles}} \times 100\% \quad (5)$$

$$C_{CH_4} = \frac{\text{converted } CH_4 \text{ in moles}}{CH_4 \text{ input in moles}} \times 100\% \quad (6)$$

$$Y_{CO}\ (\%) = \frac{\text{CO produced in moles}}{CH_4 \text{ input in moles} + CO_2 \text{ input in moles}} \times 100\% \quad (7)$$

$$Y_{H_2}\ (\%) = \frac{\text{produced in moles of } H_2}{2 \times CH_4 \text{ input in moles}} \times 100\% \quad (8)$$

$$S_{CO}\ (\%) = \frac{\text{CO produced in moles}}{CH_4 \text{ converted in moles} + CO_2 \text{ converted in moles}} \times 100\% \quad (9)$$

$$S_{H_2}\ (\%) = \frac{H_2 \text{ produced in moles}}{2 \times CH_4 \text{ converted in moles}} \times 100\% \quad (10)$$

$$\frac{H_2}{CO} = \frac{H_2 \text{ produced (mol s}^{-1})}{CO \text{ produced (mol s}^{-1})} \quad (11)$$

$$B_{carbon}\ (\%) = \frac{[CH_4]_{out} + [CO_2]_{out} + [CO]_{out}}{[CH_4]_{in} + [CO_2]_{in}} \times 100 \quad (12)$$

3. Results and discussion

3.1 Material characterization

The XRD profile of the CeO_2 NR supported Ni–Ru bimetallic catalyst is shown in Fig. 2(a). Fig. 2(a) exhibits a major phase corresponding to the face-centered cubic fluorite structure of CeO_2 with the space group of *Fm*3*m* (JCPDS #34-0394). The observed peaks at 28.5°, 33.1°, 47.5°, 56.3°, 59.1°, 69.4°, 76.7°, and 79.1° correspond to (111), (200), (220), (311), (222), (400), (331), (420), and (422) planes of the CeO_2 structure, respectively. As seen, 14 wt% NiO–1 wt% RuO_2/CeO_2 NR exhibits broad and less intense peaks, indicating that the crystallite size is small. With the help of the Scherrer formula and XRD peak assessment, the size of the CeO_2 crystallite was determined to be

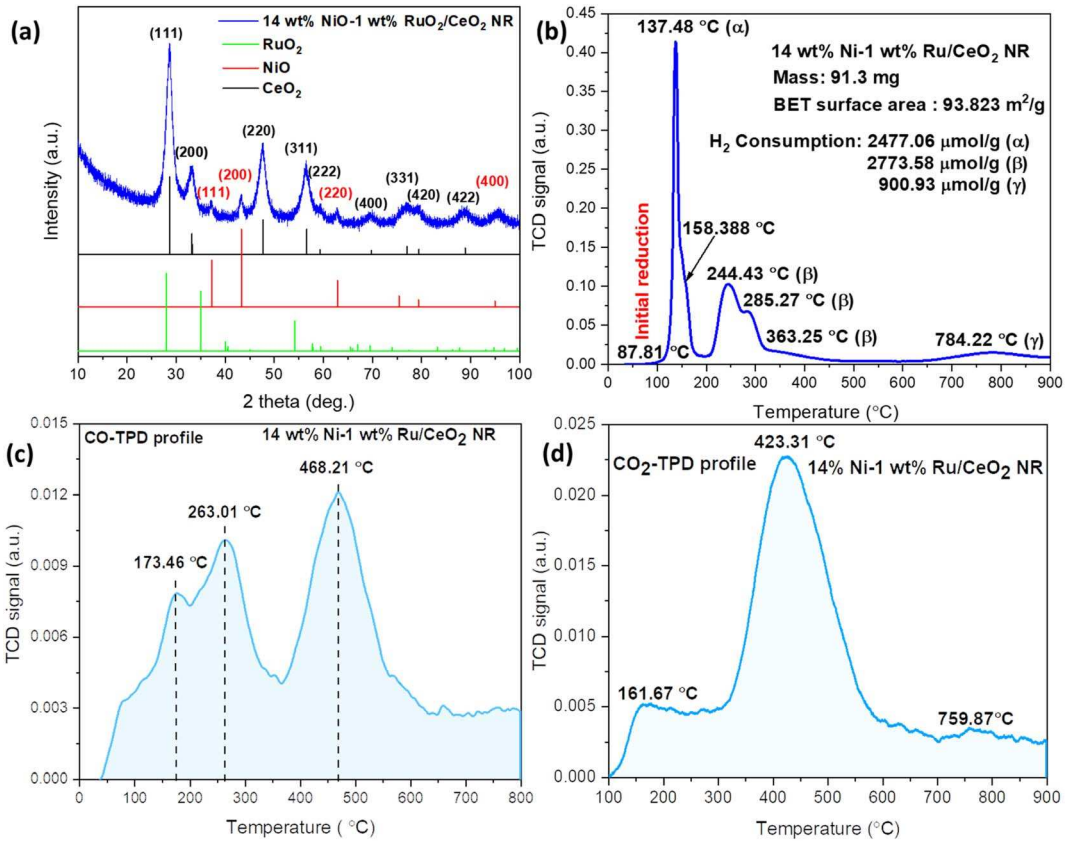

Fig. 2 (a) XRD pattern, (b) H_2-TPR, (c) CO-TPD, and (d) CO_2-TPD profiles of the fresh 14 wt% NiO–1 wt% RuO_2/CeO_2 NR catalyst.

~4 nm. Although an independent RuO_2 phase could not be distinguished on XRD, multiple tiny peaks at 2θ of ~37°, 43°, 63°, and 95° suggest the existence of NiO (JCPDS #47-1049) in the 14 wt% NiO–1 wt% RuO_2/CeO_2 NR.[21,22] The observed data indicates that NiO nanoparticles have a size of about 2 nm. The formation of Ni–Ru–Ce–O solid solution or NiO and RuO_2 diffusion into the CeO_2 NR lattice might explain the lack of RuO_x ($0 \leq x \leq 1$) and broader NiO diffraction peaks in the XRD pattern. The small RuO_2 loading (1 wt%) is also a possible reason for the absence of the RuO_x phase. Fig. 2(b) shows the H_2-TPR profile of the 14 wt% NiO–1 wt% RuO_2/CeO_2 NR catalyst. As reported in our previous experiment,[23] the reduction peaks (or H_2 consumption peaks) of CeO_2 NR occur between 300 °C and 600 °C, assigned as β-type phases, and a high temperature (>600 °C) bulk reduction peak of Ce^{4+} is assigned as γ phase. The typical H_2 consumption by CeO_2 NR starting at about 300 °C is ascribed to the surface reduction from Ce^{4+} to Ce^{3+}. However, incorporating Ni and Ru enhances the low temperature reduction of CeO_2 over the surface, which takes place at temperature below 300 °C. In the region below 200 °C (α peak), the 14 wt% NiO–1 wt% RuO_2/CeO_2 NR catalyst shows a couple of reduction peaks at 137.4 °C and 158.3 °C as a consequence of the Ni–Ru–Ce–O solid solution and multiple oxidation states of RuO_x due to the chemical linking between RuO_x and CeO_2.[24] At temperatures between 200 and 600 °C, two reduction peaks overlap the region for NiO reduction at about 244.4 °C and 285.2 °C, represented by β.[25] These peaks are assigned to the reduction of NiO, following the literature values.[26] The bimetallic 14 wt% NiO–1 wt% RuO_2/CeO_2 NR sample exhibits a low-temperature NiO reduction peak at 285.2 °C compared to the monometallic NiO/CeO_2 NR sample at 356 °C.[27] This observation agrees with the literature data,[28] demonstrating that Ru can aid in the reduction of NiO and CeO_2 as a result of hydrogen spillover. In general, the α and β peaks are attributed to the reduction of the Ru and Ni incorporated in the CeO_2 lattice or the Ru–Ni–O–Ce solid solution. The solid solution is formed by replacing Ce^{4+} with Ru^{n+} and Ni^{2+}, which generates a charge imbalance and lattice distortions within the CeO_2 NR lattice, developing high-concentration oxygen vacancies. Another high-temperature reduction peak, denoted by γ, is observed at 784.2 °C, which is assigned as the bulk reduction of CeO_2 NR.[29] Hence, it is clear that the low temperature lattice oxygen release capability of bimetallic 14 wt% NiO–1 wt% RuO_2/CeO_2 NR is significantly improved compared to the CeO_2 NR supported monometallic catalyst counterparts, which is beneficial to low-temperature DRM.[30] For better comparison, the H_2-TPR, CO_2-TPD and CO-TPD profiles of the CeO_2 NR support, NiO, RuO_2, 15 wt% NiO/CeO_2 NR, 1 wt% RuO_2/CeO_2 NR and 14 wt% NiO–1 wt% RuO_2/CeO_2 NR are presented in the ESI (Fig. S9 to S11).†

CO is one of the crucial products of the DRM reaction. Therefore, the CO-TPD profile of the 14 wt% NiO–1 wt% RuO_2/CeO_2 NR catalyst is presented in Fig. 2(c). Three desorption peaks were observed at temperatures of 173.4 °C, 263 °C, and

468.2 °C. Here, lower temperature peaks (<400 °C) are attributed to the desorption of weakly adsorbed CO species, while higher temperature peaks (>400 °C) are attributed to the desorption of strongly adsorbed CO species.[31] For instance, Li *et al.*[32] reported that adding a rare earth (La) promoter to the Ni catalyst increases the d-electron density of Ni. The weakened ability to accept paired electrons from CO reduces CO adsorption over the catalyst surface. Therefore, CO desorption is easier on the surface of Ni catalysts with a rare earth promoter, hindering the CO disproportionation. They concluded that the resistance to carbon deposition is, accordingly, extensively promoted. As shown in Fig. 2(c), similarly, due to the Ni–Ru synergism and strong metal (Ni/Ru)–support (CeO_2) interaction, the 14 wt% NiO–1 wt% RuO_2/CeO_2 NR catalyst demonstrates superior low-temperature CO desorption behavior compared to Li *et al.*'s results.[24] Thus, the possibility of carbon deposition over the surface of the CeO_2 NR supported Ni–Ru bimetallic catalyst is smaller.

It is worth mentioning that the DRM reaction starts with acid–base interactivity, in which the acid draws towards the base where the catalyst behaves as a base and CO_2 as an acid. Hence, the activation of CO_2 (acidic nature) varies on the surface of the catalyst, which regulates the stability of the catalyst and the amount of conversion. Thus, CO_2-TPD experiments were performed to get a deeper insight into the CO_2 adsorption and desorption behavior and the nature of the various basic sites on the synthesized catalyst. As shown in Fig. 2(d), the CO_2-TPD profile demonstrates the surface basicity characteristics of the CeO_2 NR supported Ni–Ru bimetallic catalyst. Three distinct desorption peaks were visible in the CO_2-TPD pattern, which ranged in temperature from 100 to 900 °C. These peaks in Fig. 2(d) are associated with the chemisorption of CO_2, which consists of three essential group class contributions, corresponding to (1) weak Brønsted basic sites (such as surface OH groups), (2) medium-strength Lewis basic sites, and (3) strong basic sites represented by low-coordination oxygen anions.[33] Thus, those three desorption peaks were observed at three temperature zones: 161.6 °C, 423.3 °C, and 759.8 °C, corresponding to weak, moderate, and strong basic sites, respectively, as depicted in Fig. 2(d). According to the literature, at 100–200 °C and 300–500 °C, the weak and moderate adsorptions correlate to the development of bridging and bidentate carbonates, respectively.[34,35] The formation of carboxylate and monodentate carbonates is responsible for the high-temperature peaks at >500 °C (strong adsorption).[36] As shown in Fig. 2(d), it is clear that the amount of CO_2 absorbed by moderate sites centered at 423.3 °C was far more significant than that of weak and strong basic sites. As pointed out in the literature,[37,38] catalysts with medium strength Lewis acid–base basic sites perform better for CO_2 absorption and activation as

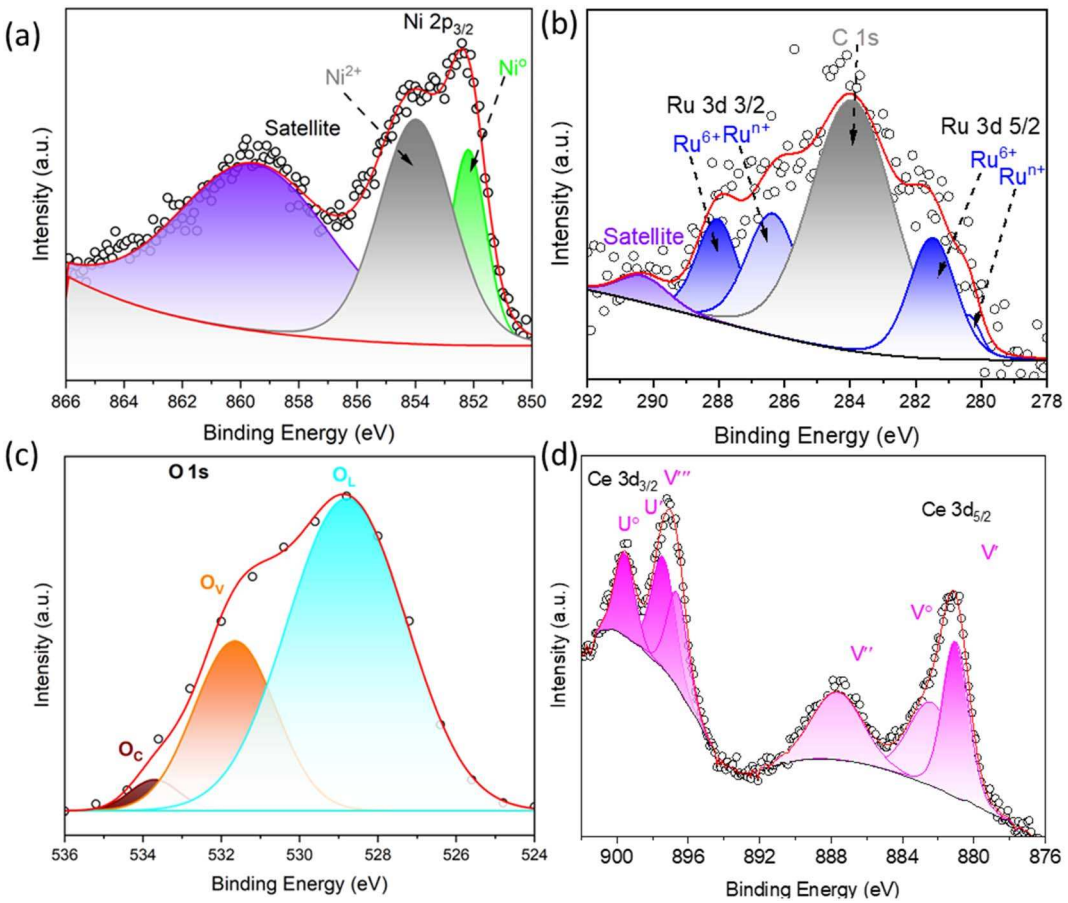

Fig. 3 XPS spectra of (a) Ni 2p, (b) Ru 3d, (c) O 1s, and (d) Ce 3d for the 14 wt% Ni–1 wt% Ru/CeO_2 NR catalyst.

well as coke resistance. These sites promote the chemisorption of acidic CO_2 and the reaction between CO_2 and CH_4, thereby facilitating the desired reforming reactions and minimizing coke formation according to the following reverse Boudouard reaction:

$$CO_2 + C = 2CO \quad (13)$$

Desorption of CO_2 on weak and moderately basic sites increases the production of active carbonate species at the metal–support interface. In contrast, desorption of CO_2 on strong basic sites may cause rapid breakdown of CH_4 and carbon deposition on active metal catalysts. The intermediate active carbonate species can produce CO *via* the interaction of O from carbonate species and C from CH_4 breakdown through the reaction with CH_4. Nevertheless, the residual carbonate species can also generate CO gas. According to the literature, CO_2 activation is easier on medium-strength basic sites than strong basic sites.[39] Thus, the low temperature and Lewis acid–base medium strength desorption peaks reveal significantly moderate basic sites, indicating a strong synergistic effect on the catalyst, hence accelerating DRM.

XPS characterization was performed to comprehend the valence states of Ni and Ru as well as the surface chemistry of the catalysts. Fig. 3(a)–(d) shows the XPS profiles of the 1s orbital of O, the 2p orbital of Ni, and the 3d orbitals of Ru and Ce. The Ni 2p orbital for the 14 wt% Ni–1 wt% Ru/CeO_2 NR catalyst in Fig. 3(a) shows multiplet splitting peaks with two different components. These two peaks are attributed to Ni–Ni or Ni^0 and Ni–O or Ni^{2+}. The recorded binding energies (BE) for these two peaks are 852.2 eV and 853.9 eV, respectively.[40] The satellite peak adjacent to the main peaks is observed at BE = 860 eV. The Ru 3d XPS profile reveals four distinct Ru peaks (Fig. 3(b)), which are attributed to Ru^{6+} $3d_{3/2}$, Ru^{n+} $3d_{3/2}$ ($4 < n < 6$), Ru^{6+} $3d_{5/2}$, and Ru^{n+} $3d_{5/2}$ ($4 < n < 6$), respectively. The Ru^{6+} peaks appeared at 280.7 eV and 288 eV, while the Ru^{n+} peaks appeared at 280.2 eV and 286.2 eV. These intense peaks coincide with the C 1s peak at 284.1 eV. The presence of Ru^{n+} peaks suggests that electrons may be transferred from RuO_x to NiO_x or CeO_{2-x}, promoting the solid solution formation of Ru–Ni–O–Ce and/or increasing oxygen vacancy concentration.[41] In Fig. 3(c), the deconvolution of the broad O 1s peak reveals multiple oxygen states, which are assigned to lattice oxygen (O_L), oxygen vacancies (O_V), and hydroxyl oxygen or chemisorbed oxygen (O_C), centered at 528.1 eV, 531.6 eV, and 533.8 eV, respectively. The percentage of these oxygen-related species is estimated using the following formula, which results in a relative oxygen vacancy concentration of 28.3%.

$$[O_V]\% = [O_V/(O_V + O_L)] \times 100 \quad (14)$$

This result indicates that a large amount of oxygen vacancies may aggregate on the surface of the 14 wt% Ni–1 wt% Ru/CeO_2 NR catalyst and stimulate the DRM reaction. It is believed that the low-temperature H_2 consumption at α and β peaks shown in Fig. 2(b) is related to these surface oxygen defects (Fig. 3(c)).

Fig. 3(d) illustrates the deconvoluted core level spectrum of Ce 3d for the CeO_2 NR supported Ni and Ru catalyst. The data shows that Ce^{4+} 3d presents four distinct peaks at 881 eV, 887.7 eV, 896.6 eV, and 897.5 eV, denoted by V′, V″, V‴, and U′, respectively. U and V represent the Ce $3d_{3/2}$ and Ce $3d_{5/2}$ states, respectively. The presence of Ce^{3+} ions originating from Ce $3d_{5/2}$ and Ce $3d_{3/2}$ is responsible for the peaks at 882.5 eV (V°) and 899.5 eV (U°), respectively. According to the literature, Ce^{3+} strongly indicated the formation of oxygen vacancies, which is also acknowledged by the deconvolution of the O 1s peak in Fig. 3(c).[42,43] The formation of oxygen vacancies is crucial in the context of DRM reaction, particularly for catalytic stability and performance. The relative Ce^{3+} ion concentration can be computed by integrating each peak area, using the following formula:

$$[Ce^{3+}]\% = \frac{A_{U^\circ} + A_{V^\circ}}{A_{U^\circ} + A_{V^\circ} + A_{U'} + A_{V'} + A_{V''} + A_{V'''}} \times 100 \quad (15)$$

The calculation shows that the relative Ce^{3+} ion concentration is 37.23% (Table 1). Thus, due to the different valence states and coordination number with oxygen, the Ru and Ni loading on the CeO_2 NR support leads to undercoordinated Ce^{3+} ions and oxygen vacancies (Fig. 3(c)).

The low and high-resolution TEM images of the CeO_2 NR supported Ni and Ru catalyst are shown in Fig. 4 at different magnifications. The prepared bimetallic catalyst exhibits a rod-shaped structure with little aggregation, as clearly observed in Fig. 4. Thus, it is apparently clear that the CeO_2 support retained its rod-like or initial morphology even after the Ni–Ru loading and calcination. The length of the CeO_2 NR sample ranges

Table 1 XPS peak assignment, position and relative area of Ce 3d

Sample ID	Peak assignment	Ce species	Binding energy (eV)	Relative area (%)
CeO_2	V°	Ce^{3+}	882.5	23.3
	V′	Ce^{4+}	881.0	15.1
	V″	Ce^{4+}	887.7	22.6
	V‴	Ce^{4+}	896.6	12.6
	U°	Ce^{3+}	899.5	14.1
	U′	Ce^{4+}	897.5	12.4

Percentage of Ce^{3+} = 37.2%
Percentage of Ce^{4+} = 62.8%

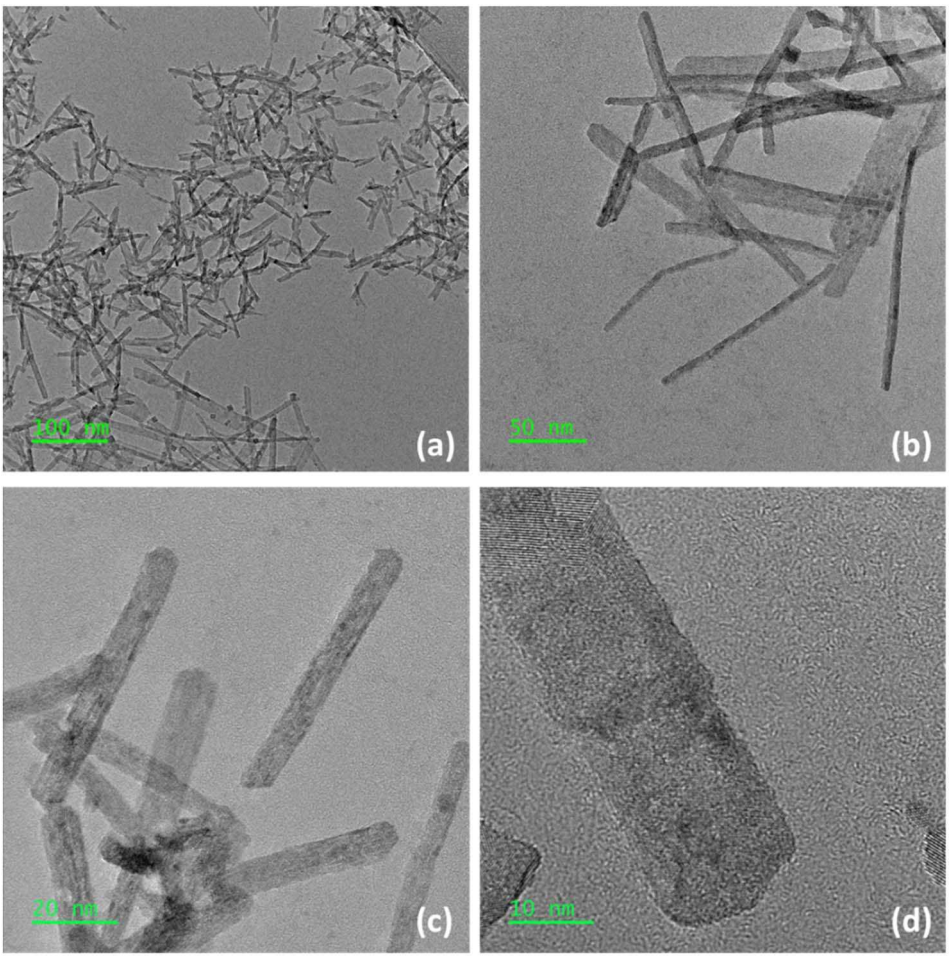

Fig. 4 HRTEM images at different magnifications (a–d) for the 14 wt% NiO–1 wt% RuO_2/CeO_2 NR catalyst.

between 70 and 120 nm, while the diameter is in the range between 5 and 15 nm. The lattice fringe of CeO_2 NR with a *d*-spacing of 3.08–3.12 Å is consistent with the (111) crystal plane. Additionally, the CeO_2 NR support's rough texture revealed by the HRTEM images indicates the existence of lattice defects, lattice distortion, voids, and other surface imperfections/defects.

3.2 Catalyst performance test

A typical redox cycle experimental result obtained at 400 °C, measured by using an Extrel QMS, is shown in Fig. 5(a). The experimental process shown in Fig. 5(a) contains three repetitions followed by a 75 minute reduction cycle in the last section to test the catalyst stability. As shown in Fig. 5(a), the mole concentrations of CO_2, CH_4, CO, H_2, and O_2 exhibit a similar pattern over time, during each of the three cycles. In the third section for the stability test, under plasma-assisted catalytic conditions, the concentrations of CO and H_2 gases exhibit stable production of 48% and 25%, respectively, without any apparent change from 85 min to 145 min (60 minutes). Fig. 5(b) depicts the molar percentage of CH_4, CO_2, CO, and H_2 measured from the Extrel QMS for DRM at seven different temperatures ranging from 150 to 450 °C during the reduction cycle. The effect of adding plasma to the thermal DRM is clearly depicted in Fig. 5(b), with two separate colors representing the thermal and thermal + plasma portions. For each 12 minute reduction cycle, the thermal DRM response lasts for the first five minutes, followed by the plasma + thermal response for the next seven minutes, beginning at the 6^{th} minute and continuing until the 12^{th} minute. Thus, during 12 minutes of reduction, the plasma generator is turned OFF for the first 5 minutes and ON for the rest of the 7 minutes. This "plasma-OFF plasma-ON" study aimed to determine the synergistic effect of plasma + thermal DRM catalysis. The plasma temperature during reaction was separately measured using a thermopile infrared array sensor (Model: HTPA 32*32d) and an infrared thermometer (Model: IT-T04). The measurement showed that both measurements indicated a temperature of 480–490 °C at a furnace temperature of 450 °C. During the first 5 minutes of thermal catalysis at 150 °C, neither CO nor H_2 was initially detected due to the thermodynamic barrier of the DRM reaction. However, as soon as the plasma was initiated (plasma-ON) at the 6^{th} minute, the indicator of CO (green line) and H_2 (blue line) gases become clearly apparent. Simultaneously, there is an abrupt drop in the mole concentrations of the reactants CO_2 (red line) and CH_4 (black line). The initial mole percentage of

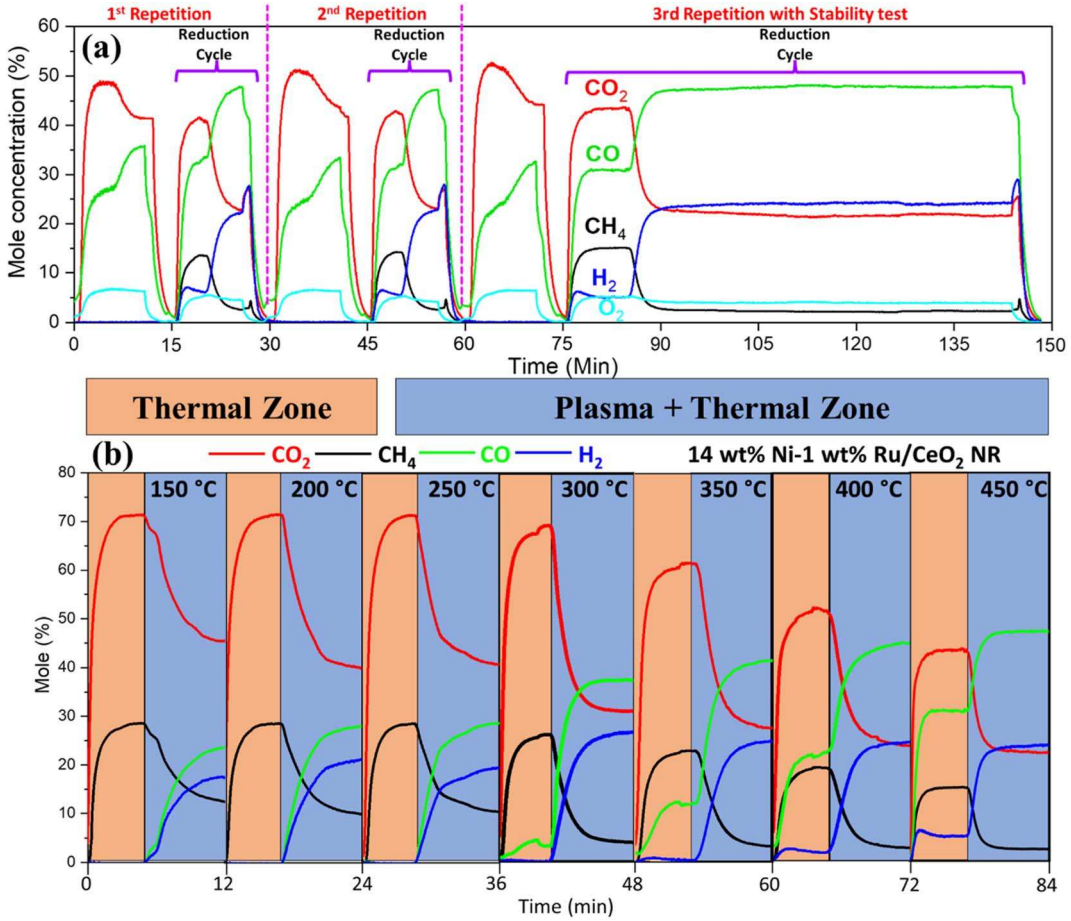

Fig. 5 Measurement of time-resolved species in mole fraction for (a) a complete cycle with three repetitions at 400 °C and (b) for thermal and thermal + plasma regions from temperature between 150 °C and 450 °C at 1 atm pressure (5 minutes for only thermo-catalytic DRM and 7 min for thermal and plasma-catalytic DRM) (catalyst weight: ~200 mg, flow rate: CO_2: 250 sccm and CH_4: 100 sccm, plasma power: 17.66–22.73 W, and frequency: 20 kHz).

CO and H_2 in the thermal catalysis region at 150 °C was "zero" before the plasma was turned on, but it increased to 24% and 18%, respectively. CO and H_2 were not visible until 300 °C for thermally driven DRM. However, in the thermal + plasma regions, the mole fractions of CO and H_2 climbed to 38% and 27%, respectively, from 150 °C to 300 °C. This demonstrates the vital role of plasma in triggering and driving the low-temperature reaction of DRM to syngas. In thermal DRM, with increasing temperatures up to 450 °C, the mole concentrations of CO and H_2 reach a maximum of 31% and 5%, respectively. However, in the thermal + plasma DRM at 450 °C, the CO and H_2 concentrations are 47% and 24%, respectively, which are substantially higher than those in the thermal-only DRM sections.

The plasma-assisted DRM was performed with a mixing ratio of $CO_2/CH_4 = 250:100$ and a total flow rate of 350 sccm. The primary products of the DRM reaction are hydrogen (H_2) and carbon monoxide (CO), with some ethane (C_2H_6) also being produced in trace amounts. The influence of temperature on the plasma-catalytic DRM is depicted in Fig. 6. The overall conversion of CH_4 and CO_2, yield and selectivity of CO and H_2, H_2/CO ratio, and carbon balance from thermal and plasma-assisted catalytic DRM are illustrated in Fig. 6 and 7 for two different power levels, 8.85–11.35 W and 17.66–22.73 W, respectively, at distinct temperatures. Compared to the thermo-catalytic DRM, the addition of plasma (power: 8.85–11.35 W) with the 14 wt% Ni–1 wt% Ru/CeO_2 NR catalyst dramatically increased conversions, with the maximum CH_4 and CO_2 conversions reaching 58% and 40%, respectively, at 450 °C. It is crucial to note that due to the endothermic characteristic of the DRM process, no reaction occurred in thermal DRM until 350 °C,[44] which is in line with the report by Horlyck, J. *et al.*[45] The conversion of CH_4 and CO_2 was typically observed in thermal-driven DRM with the pure Ni catalyst at operating temperatures greater than 300 °C.[46] Thus, plasma-assisted thermo-catalytic DRM had a trigger temperature at least 250 °C lower than that of thermal DRM. For example, from Fig. 6(a) and (b), in thermally driven DRM, CH_4 and CO_2 conversion climbed to a maximum of 26% and 15%, respectively, at 450 °C. However, similar conversions were obtained at around 200 °C in a plasma-assisted environment. Under the conditions of NTP, the frequency of collisions among gas molecules and electrons rapidly rises, contributing to the formation of more reactive species, such as radicals and ions. For instance, the reactant

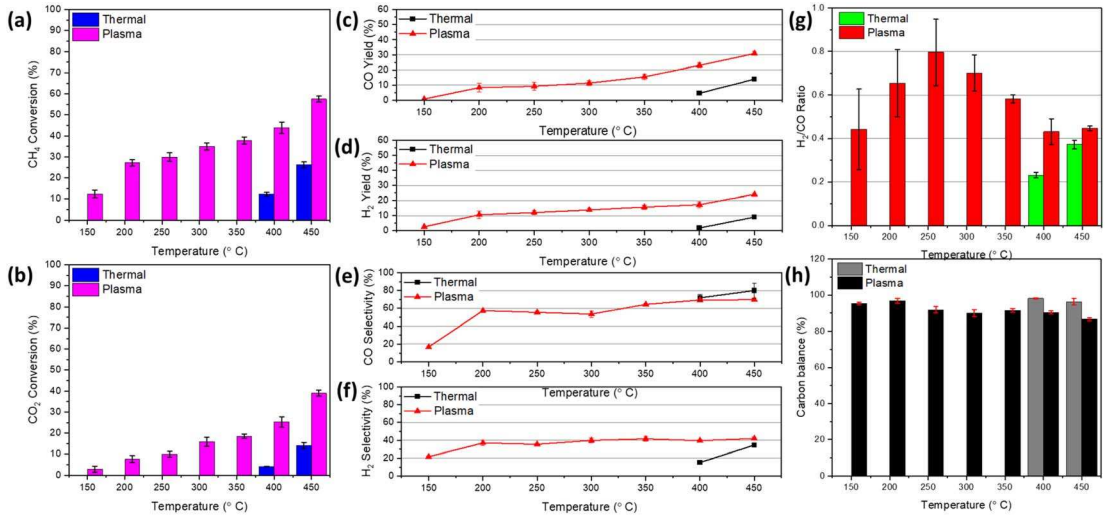

Fig. 6 Thermal and plasma-catalytic DRM conversion of 14 wt% Ni–1 wt% Ru/CeO_2 NR between 150 °C and 450 °C at 1 atm pressure: (a) CH_4 conversion, (b) CO_2 conversion, (c and d) CO and H_2 yield, (e and f) CO and H_2 selectivity, (g) H_2/CO ratio, and (h) carbon balance (catalyst weight: ~200 mg, flow rate: CO_2: 250 sccm and CH_4: 100 sccm, plasma power: 8.85–11.35 W, and frequency: 20 kHz).

CH_4 can split into active H atoms and CH_x ($x = 0$, 1, 2, and 3), which are then coupled with products from the cracking of CO_2 to generate products like CO and H_2.[47] Thus, for plasma-assisted catalytic DRM at a constant power of 8.85–11.35 W, a notable enhancement in CH_4 and CO_2 conversions was observed. More specifically, CH_4 conversion increased from 13% to 58%, while CO_2 conversion increased from 4% to 39%. This improvement occurred over the temperature range of 150 to 450 °C using the 14 wt% Ni–1 wt% Ru/CeO_2 NR catalyst. The rise in temperature is subject to an increase in CO and H_2, yield and selectivity, as seen in Fig. 6(c)–(f). The maximum CO selectivity and yield were 70% and 30%, respectively, for plasma-assisted DRM, while for thermal catalytic DRM, these values were 80% and 14% at 450 °C. Similarly, the maximum H_2 selectivity and yield were 41% and 25%, respectively, for plasma-assisted DRM, which is higher than those in thermally driven DRM (H_2 selectivity: 34% and yield: 10%) at 450 °C. Due to the production of hydrocarbons, CO exhibits better selectivity than H_2.[48] It should be noted that CO and H_2 yield in thermal catalytic DRM is low, with a maximum of 14% and 10%, respectively, due to the low conversion of CH_4 and CO_2. In Fig. 6(g), the H_2/CO ratio is <1, indicating that more CO was produced than H_2, likely due to some side reactions.[49] For instance, the reverse water gas shift (RWGS) reaction in eqn (16) may cause a lower H_2/CO ratio, a frequent occurrence in thermal or plasma catalytic DRM.[48]

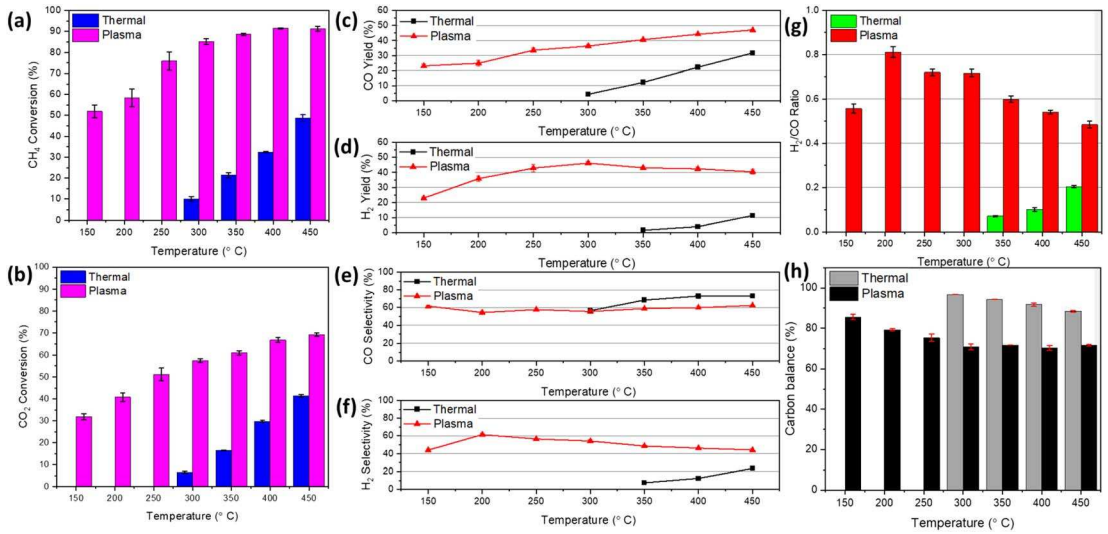

Fig. 7 Thermal and plasma-catalytic DRM conversion of 14 wt% Ni–1 wt% Ru/CeO_2 NR between 150 °C and 450 °C at 1 atm pressure: (a) CH_4 conversion, (b) CO_2 conversion, (c and d) CO and H_2 yield, (e and f) CO and H_2 selectivity, (g) H_2/CO ratio, and (h) carbon balance (catalyst weight: ~200 mg, flowrate: CO_2: 250 sccm and CH_4: 100 sccm, plasma power: 17.66–22.73 W, and frequency: 20 kHz).

$$CO_2 + H_2 = CO + H_2O;\ \Delta H_{298\ K} = 41.2\ kJ\ mol^{-1} \quad (16)$$

So this side reaction might utilize the H_2 produced, lowering the H_2 yield and increasing CO generation. The carbon balance for thermal and plasma-driven DRM at various temperatures is also exhibited in Fig. 6(h). Clearly, carbon balance is close to 100% at lower temperatures, while at higher temperatures, it is less than 90%. The observation demonstrated the high temperature-induced carbon deposition. The QCL system identified a negligible amount of C_2H_6 (1.16%) at 150 °C, which decreased with increasing temperature.

In plasma-assisted catalytic DRM, discharge power is proportional to the electric field strength in the plasma region and causes highly excited electrons to collide inelastically with reactant molecules. Greater discharge power enhances the number of micro-discharges and determines the number of reactive radicals. Fig. 7 depicts the corresponding plasma-assisted DRM performance at a constant power range of 17.66 to 22.73 W for temperatures ranging from 150 °C to 450 °C. Compared to Fig. 6, Fig. 7 demonstrated a high-power effect in plasma-assisted DRM performance. Fig. 7(a) and (b) shows the experimentally observed CH_4 and CO_2 conversion across a range of temperatures for thermal and plasma-assisted DRM tests. At this power (17.66 to 22.73 W), the CH_4 conversion increased from 52% to 92% from 150 to 450 °C. On the other hand, the CO_2 conversion climbed from 32% to 70% in the same temperature range.

Plasma-assisted DRM can start converting gases at temperatures as low as 150 °C, while thermal DRM does not work until temperatures reach about 300 °C. Furthermore, it is shown that the conversion rate of CO_2 was lower than that of CH_4. Because CH_4 has a lower binding energy than CO_2, increasing its adsorption on catalyst surfaces accelerates CH_4 conversion, as discussed previously. According to the literature, the rate of CH_4 conversion is higher when the $CH_4 : CO_2$ feed gas ratio is less than 1, which could be due to excess O_2.[50] Istadi *et al.*[51] noticed that a greater CO_2 concentration promotes the CH_4 conversion. Plasma-catalytic synergism and their interaction with reactant gas molecules generate methyl/hydrocarbon radicals from CH_4 and reactive metastable $O(^1D)$ from CO_2 dissociation, enabling the co-feed to enhance the conversion. Fig. 7(c)–(f) depicts the yield and selectivity of CO and H_2, respectively, as a function of temperature for both thermal and plasma-assisted DRM. The maximum obtained CO and H_2 yields were 47% and 45%, respectively, while CO and H_2 yields reached 31% and 11% in thermally driven DRM, respectively. Thus, introducing plasma leads to higher CO_2 and CH_4 conversion, increasing the yield of CO and H_2 compared to thermal catalytic DRM. It is noticeable from Fig. 7(d) that H_2 yield initially increased with temperature up to 300 °C. However, the trends changed in a downward direction at higher temperature. This finding can be explained by Fig. 7(a), where CH_4 conversion is close to constant with a value of 87% to 92%. Hence, it can be concluded that at 300 °C, CH_4 reached its maximum conversion with the maximum yield. However, temperatures above 300 °C may change the reaction toward forming hydrocarbons, or C2 species, rather than H_2. This is also clear from the H_2/CO ratio and carbon balance graph in Fig. 7(g) and (h). The maximum H_2/CO ratio at a constant power of 17.66 to 22.73 W and a temperature of 200 °C is 0.81. As seen from Fig. 7(g) and (h), the H_2/CO ratio and carbon balance decrease with temperature

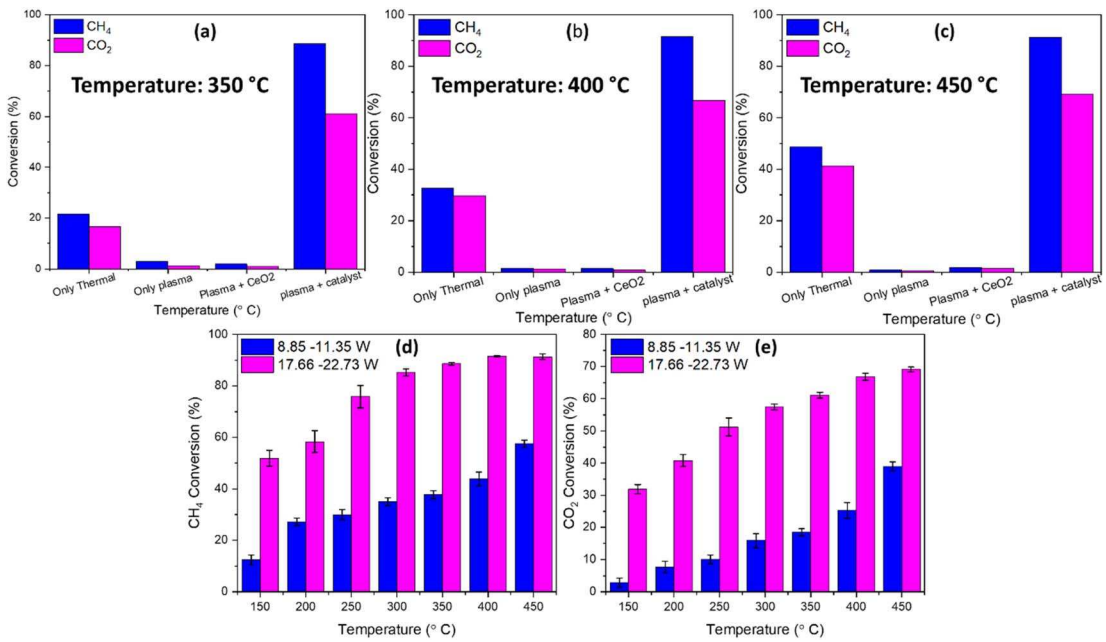

Fig. 8 Comparison plot of CH_4 and CO_2 conversion at (a) 350 °C, (b) 400 °C, and (c) 450 °C with thermal only, plasma only, plasma with the bare CeO_2 NR support and plasma with the catalyst, and (d) CH_4 and (e) CO_2 conversion with two different applied plasma discharge powers (catalyst weight: ~200 mg, flow rate: CO_2: 250 sccm and CH_4: 100 sccm, and frequency: 20 kHz).

above 200 °C, indicating the formation of by-products. Tu *et al.*[52] concluded that the reverse Boudouard reaction in eqn (8) produces more CO due to the reaction between deposited carbon and CO_2 and leads to a low syngas ratio. As shown in Fig. S8,† the HRTEM images of the spent catalyst showed the formation of carbon nanotubes while the shape of the support is unchanged. The changes in CO and H_2 selectivity, which represent the formation of desirable CO and H_2 in secondary product formation, are shown in Fig. 7(e) and (f). Notably, CO selectivity was stable (~60%), while H_2 selectivity reached 60% at 200 °C.

Fig. 8(a)–(c) compares the CH_4 and CO_2 conversion based on thermal only, plasma only, plasma + support, and plasma + catalyst at different temperatures, while Fig. 8(d) and (e) presents the CH_4 and CO_2 conversion in two different power ranges 8.85–11.35 W and 17.66–22.73 W, respectively, from 150 °C to 450 °C. It is noticeable from Fig. 8(a)–(c) that introducing plasma enhances the CH_4 and CO_2 conversion significantly compared to thermal only, plasma only, or plasma with bare support. Furthermore, the temperature increment to 50 °C induces the reaction collision and promotes higher conversion. Conversely, applied plasma discharge power plays a crucial role in CH_4 and CO_2 conversion, as shown in Fig. 8(d) and (e). The conversion, carbon balance, mole percentage, yield, and selectivity of CO and H_2 of DRM reaction under plasma only and plasma with bare support are added in the ESI (Fig. S5 and S6).† It is important to note that a slight variation of plasma power was observed during the reaction while the source was set to a constant voltage. The voltage and current graph of plasma power and its properties are included in Fig. S12 and Table S1.† The increasing plasma power from the range 8.85–11.5 W to 17.66–22.73 W increases the conversion by at least 30%, which can be attributed to the enhanced collision frequency of electrons, ions, and radicals and promotes the conversion of CH_4 and CO_2.

The plasma-catalytic DRM stability of the 14 wt% Ni–1 wt% Ru/CeO_2 NR catalyst was evaluated at a power of 17.66 to 22.73 W with an external temperature of 350 °C over 75 minutes. The total flow rate of 350 sccm and feed gas ratio of 0.4 (CH_4 : CO_2 = 100 : 250) are maintained. As shown in Fig. 9, the CH_4 and CO_2 conversion percentages and carbon balance are stable with time in a plasma-assisted environment. Significant variations in the reactant conversions occurred during the first 10 minutes of reaction due to the unstable reactant concentration at the beginning of the reaction. However, the percentage difference between the two values collected 60 minutes apart was less than 4%. The 14 wt% Ni–1 wt% Ru/CeO_2 NR catalyst exhibited stable conversions (CH_4 ~89% and CO_2 ~60%) within 60 min. The results show that stable reactant conversions were achieved due to the catalyst regeneration technique, low inert carbon deposition, or higher activated carbon deposition. The CH_4 and CO_2 conversion has slight increasing slopes, which can be attributed to plasma-catalytic synergism. A plasma-assisted environment can enhance metal dispersion over the support of the heterogeneous catalyst, start the generation of tiny metal nanoparticles, and stop nanosized catalyst particles' growth due to high temperature-induced sintering.[53] Thus, a small amount

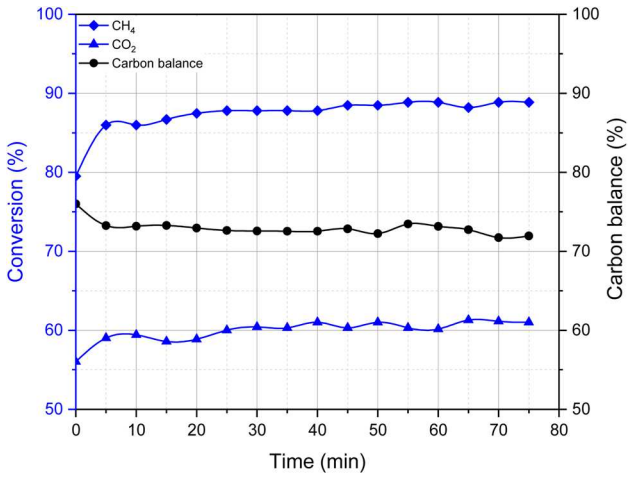

Fig. 9 Stability of the 14 wt% Ni–1 wt% Ru/CeO_2 NR catalyst at 350 °C for plasma catalytic DRM (CH_4 and CO_2) in terms of conversion and carbon balance (catalyst weight: ~200 mg, flow rate: CO_2: 250 sccm and CH_4: 100 sccm, plasma power: 17.66–22.73 W, and frequency: 20 kHz).

of Ru addition to the catalyst raises the catalytic activity dramatically compared to an individual mono-metallic catalyst.[44] This is possibly due to the greater specific surface area and qualitative metal dispersion of the smaller metal particles produced due to the catalytic plasma reaction.

Fig. 10(a)–(d) illustrates the effect of various CO_2/CH_4 feed gas ratios on the reaction of plasma-assisted catalytic DRM at 450 °C with the discharge power of 17.66 to 22.73 W. Here, a total of 350 sccm of CO_2 and CH_4 were supplied into the reactor at various ratios: 250 : 100, 200 : 150, 175 : 175, 150 : 200, and 100 : 250. The literature reports that during DRM the amount of CO_2 has a significant influence in CH_4 conversion because metastable O (^1D) molecules from CO_2 breakdown react with the C–H bond, forming ethyl radicals and hydroxyl molecules.[54,55] It is agreed that a lower CH_4 concentration (CO_2/CH_4 ratio > 1) in the feed mixture will result in a higher CH_4 conversion. In this study, at a CO_2/CH_4 ratio of 250 : 100, or 2.5, the CH_4 conversion is 92%, while the CO_2 conversion is 70%. With an increase in CH_4 feed supply, the CH_4 conversion fell from 92% (250 : 100) to 53% (100 : 250). As demonstrated by eqn (17) and (18), the excited oxygen O* dissociated from CO_2 plays a critical role in the decomposition of CH_4.

$$CH_4 + O^* = CH_3^* + OH^* \quad (17)$$

$$CH_4 + OH^* = CH_3^* + H_2O \quad (18)$$

These reactions suggest that the ratio of CO_2 to CH_4 is critical to the conversion of CH_4. With varied CO_2/CH_4 ratios, the CO_2 conversion stayed in the range of 60% and 70%. With a low CH_4 feed concentration, CO generation led to a higher CH_4 conversion because the formation of CO required the participation of more active CH_x species. However, when the total feed flow rate of CO_2 is reduced, CH_x species engage in recombination rather than oxidation to produce CO.[56]

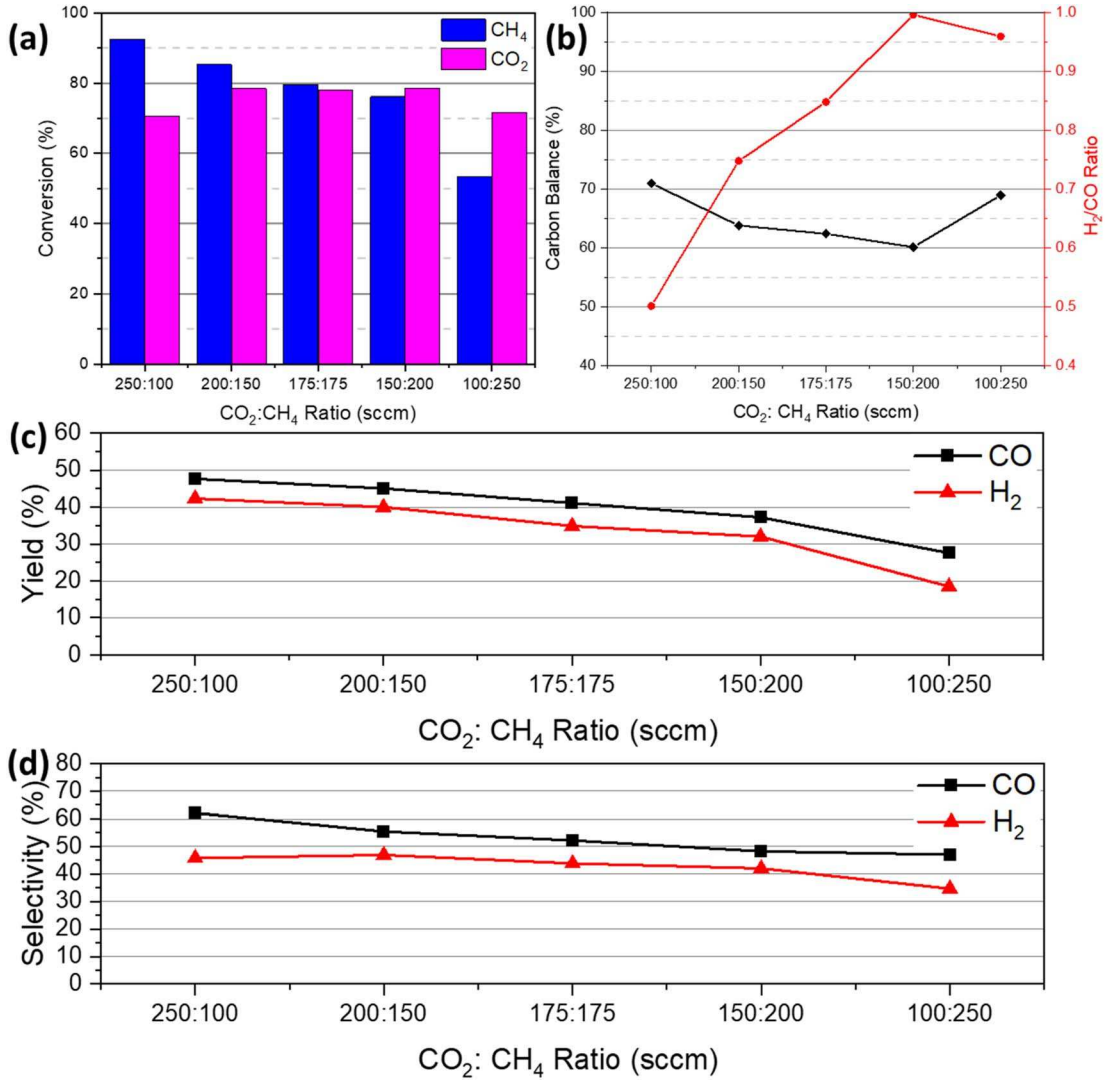

Fig. 10 Plasma-catalytic DRM conversion of 14 wt% Ni–1 wt% Ru/CeO_2 NR as a function of CO_2 : CH_4 feed gas ratio at 450 °C: (a) CH_4 and CO_2 conversion, (b) H_2/CO ratio and carbon balance, (c) CO and H_2 yield and (d) selectivity (catalyst weight: ~200 mg, total flow rate: 350 sccm, plasma power: 17.66–22.73 W, and frequency: 20 kHz).

As the ratio of CO_2 to CH_4 decreased, the total conversion rate began to decline. This is because decreasing the CO_2/CH_4 ratio reduces the amount of oxygen in the process, which stimulates the production of hydrocarbons rather than syngas, including carbon deposition, which can be observed in Fig. 10(b). This carbon deposition can result in catalyst poisoning or deactivation. Fig. 10(b) further demonstrates that the H_2/CO ratio rose as the CO_2 to CH_4 ratio decreased due to a greater concentration of CH_x species in the reaction. Fig. 10(c) and (d) presents the CO and H_2 yield and selectivity with the variation of CO_2/CH_4 ratios. Both yield and selectivity showed a downward trend with decreasing CO_2 to CH_4 feed gas ratios. The total conversion fell because of the downward ratio trend, leading to low CO and H_2 yield and selectivity.

TEM images of the spent catalyst are presented in Fig. 11. It is noticeable from Fig. 11 that carbon was deposited in the form of nanotubes. This observation is consistent with the carbon balance profile (71%), illustrated in Fig. 7(h). In addition, the RAMAN characterization of the spent catalyst confirmed that the carbon is activated carbon, as presented in the ESI (Fig. S3).†

After the DRM reaction, each catalyst underwent a regeneration cycle with CO_2 and Ar in thermal and plasma environments to recover or eliminate the carbon deposited on the catalyst's surface. Interestingly, the prepared bimetallic 14 wt% Ni–1 wt% Ru/CeO_2 NR catalyst promoted a CO_2-splitting reaction as shown in eqn (19) during this regeneration cycle, which increased its conversion with temperature.

$$CO_2 = CO + O \quad (19)$$

This increase in conversion can be attributed to the combination of furnace temperature, the effect of NTP, and the 14 wt% Ni–1 wt% Ru/CeO_2 NR catalyst. In addition, Ar acted as a highly reactive metastable species such as Ar* and Ar^+, which can enhance the collision of CO_2 and reactive species and promote CO_2 splitting in the regeneration cycle. For instance,

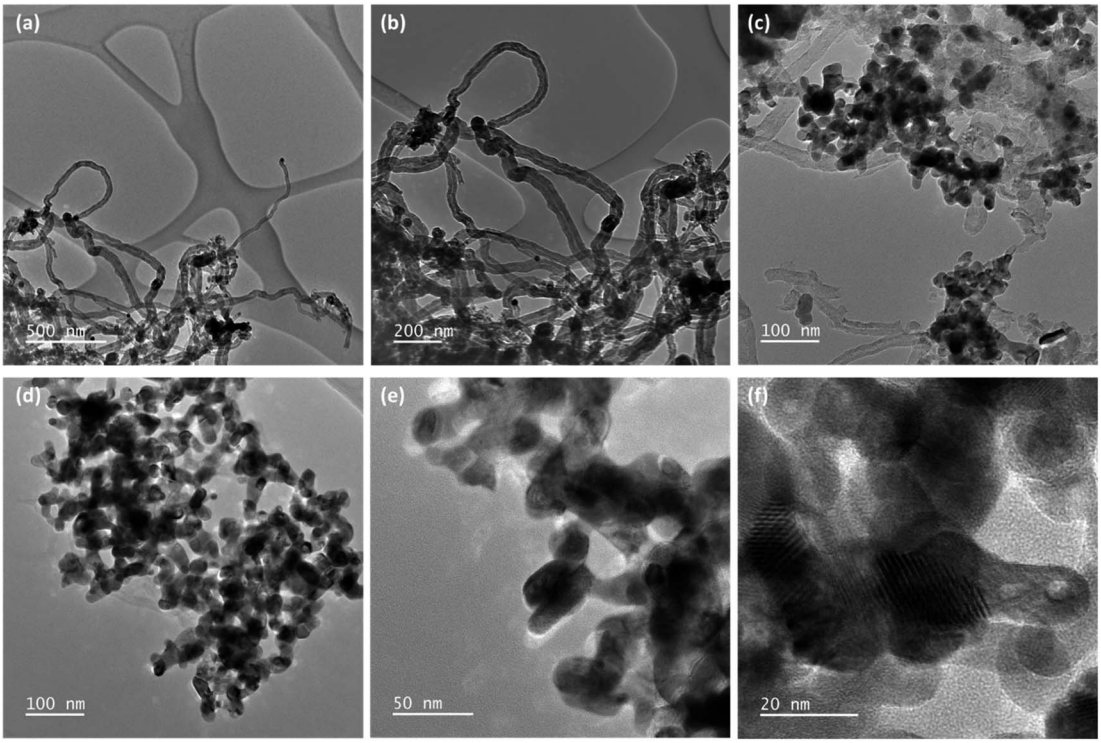

Fig. 11 TEM images at different magnifications (a–f) of the spent 14 wt% NiO–1 wt% RuO_2/CeO_2 NR catalyst.

Jahanbakhsh *et al.*[57] reported low-temperature CO_2 splitting under an NTP environment similar to the regeneration cycle of this experiment. Fig. 12(a) and (b) depicts the variation in CO_2 conversion and yield depending on the temperature in plasma and thermal only environments. With an increase in temperature from 150 °C to 450 °C under NTP catalysis, the CO_2 conversion increased, reaching a highest conversion of 40%. The CO_2 : Ar feed gas ratio was 250 : 100, similar to the DBD plasma-assisted CO_2 decomposition experiment reported by Ray *et al.*[58] They concluded that the concentration of diluent gas Ar plays a crucial role in CO_2 decomposition. It should be noted that at 150 °C and 200 °C under plasma-assisted catalytic regeneration, no CO_2 splitting reaction was observed. Similarly, no thermal CO_2 splitting was noticed up to 300 °C due to its highly endothermic nature.

4. Proposed reaction mechanism

The NTP-assisted DRM reaction routes over 14 wt% Ni–1 wt% Ru/CeO_2 NR can be explained based on the Langmuir–

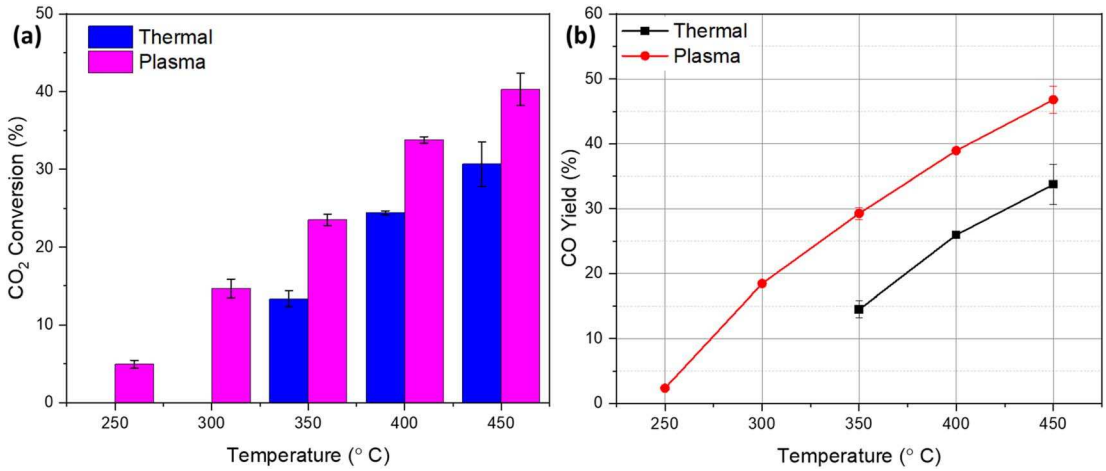

Fig. 12 Thermal and plasma-assisted CO_2 splitting reaction during the catalyst regeneration cycle of 14 wt% Ni–1 wt% Ru/CeO_2 NR from 150 °C to 450 °C: (a) CO_2 conversion and (b) CO yield (catalyst weight: ~200 mg, flow rate: CO_2: 250 sccm and Ar: 100 sccm, power: 17.66–22.73 W, and frequency: 20 kHz).

Table 2 Possible reactions of plasma-assisted DRM

Plasma enhanced CH_4 and CO_2 dissociation	
$CH_4 + e^- \Rightarrow CH_4^+ + 2e^-$	(R1)
$CH_4 + e^- \Rightarrow CH_3^+ + H + 2e^-$	(R2)
$CH_4 + e^- \Rightarrow CH_3 + H + e^-$	(R3)
$CH_4 + e^- \Rightarrow CH_2 + H_2 + e^-$	(R4)
$CH_4 + e^- \Rightarrow CH + H_2 + H + e^-$	(R5)
$CO_2 + e^- \Rightarrow CO_2^+ + 2e^-$	(R6)
$CO_2 + e^- \Rightarrow CO + O + e^-$	(R7)
$CO_2 + e^- \Rightarrow CO + O^-$	(R8)
Surface reaction	
$CO_3^{2-} + CH_x \Rightarrow CH_xO + CO + O^{2-}$	(R13)
Catalytic CH_4 and CO_2 adsorption	
$CH_4 \Rightarrow CH_x + (4 - x)H$	(R9)
$CH_4 \Rightarrow C + 4H$	(R10)
$CO_2 + O^{2-} \Rightarrow CO_3^{2-}$	(R11)
$CO_2 \Rightarrow CO + O$	(R12)
Surface desorption	
$CH_xO \Rightarrow CO + \frac{x}{2}H_2$	(R14)
$H + H \Rightarrow H_2$	(R15)
$C + M\text{–}O \Rightarrow CO + M$	(R16)
M: metal	

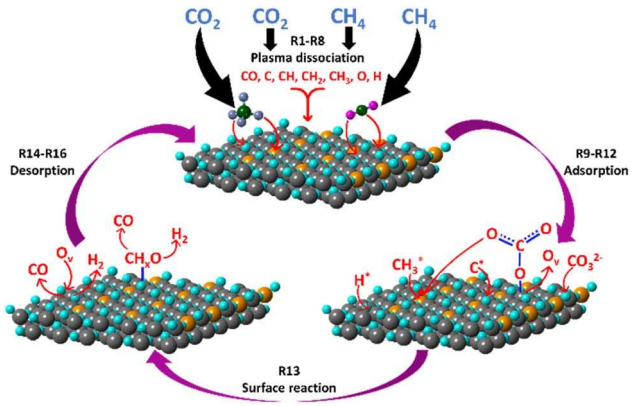

Fig. 13 Possible reaction mechanisms of plasma-assisted DRM.

Hinshelwood mechanism. First, plasma activates CH_4 and CO_2 molecules which dissociate into various electronically, vibrationally and rotationally excited intermediate species such as CH_x, CO_2^+, O, H, and CO_3^{2-} which are adsorbed on the surface of the metal and/or support.[59] According to the literature,[60] CH_4 activation is favored at metal sites, metal/support interface, or oxygen vacancies at the metal/support interface, followed by consecutive dehydrogenation. On the contrary, as an acidic species, based on the surface structure of the catalyst, CO_2 adsorbs on active species in three different ways: C coordination, C–O coordination and O coordination.[61] These adsorptions can be promoted by the surface basic sites of the catalyst, which contribute anionic oxygen (O^{2-}), leading to the formation of surface covalent carbonate species (CO_3^{2-}). These carbonate species interact with surface adsorbed CH_x ($x = 1$–3) on adjacent Ni or Ru followed by production of CO and H_2 (syngas).[62–64] The possible reactions for the first stage are given below.

Some possible reactions are given below in Table 2 and schematically shown in Fig. 13.

It is well known that the dry reforming of methane reaction favors carbon deposition or coking at higher temperatures by the following reactions.

Methane decomposition or methane cracking:

$$CH_4 = 2H_2 + C \quad (20)$$

Boudouard reaction:

$$2CO = CO_2 + C \quad (21)$$

Under the plasma environment, carbon deposition from methane cracking is mostly activated rather than Boudouard reaction.[65] This deposited carbon quite effectively reacts with oxygen radicals.[66]

5. Conclusion

In conclusion, plasma-assisted DRM was investigated in an atmospheric pressure DBD reactor using the 14 wt% Ni–1 wt% Ru/CeO_2 NR catalyst. Plasma alone or plasma with bare support did not effectively facilitate the DRM reaction, resulting in CH_4 and CO_2 conversions of less than 5% over the temperature between 150 °C and 450 °C. The results revealed that the synergy between the 14 wt% Ni–1 wt% Ru/CeO_2 NR catalyst and non-thermal plasma accelerated the surface reaction in the plasma-assisted DRM environment, resulting in a maximum 91% conversion of CH_4 and 70% conversion of CO_2, respectively, at 450 °C. Furthermore, the 14 wt% Ni–1 wt% Ru/CeO_2 NR catalyst exhibited excellent stability and less coking issue, as evidenced by its sustained conversion up to 60 min without any drop, and its morphology and shape remained unchanged due to the low reaction temperature, as verified by XRD and HRTEM analyses of the spent catalyst, respectively. The Raman spectroscopy analysis of the used catalyst verified that the deposited carbon was activated carbon. Using the 14 wt% Ni–1 wt% Ru/CeO_2 NR catalyst, the effect of the input feed gas ratio on plasma-assisted DRM was also studied. The findings demonstrated that an enhanced ratio of H_2/CO could be achieved by increasing the CH_4 feed gas percentage in the gas mixture. However, this can result in a reduced total conversion. Thus, the improved catalytic DRM performance is ascribed to the synergistic effect of non-thermal plasma and the presence of higher active sites on the CeO_2 NR supported bimetallic Ni–Ru catalyst with a significant amount of surface defects including Ce^{3+} ions, oxygen vacancies, voids, and rough support surfaces.

Data availability

The data supporting this article have been included as part of the ESI.†

Conflicts of interest

There are no conflicts to declare.

Acknowledgements

This work is funded by the National Science Foundation (CBET-2427238 and TI-2427213).

References

1 Z. Sheng, H.-H. Kim, S. Yao and T. Nozaki, Plasma-chemical promotion of catalysis for CH_4 dry reforming: unveiling plasma-enabled reaction mechanisms, *Phys. Chem. Chem. Phys.*, 2020, **22**, 19349–19358.

2 S. Hamzehlouia, S. A. Jaffer and J. Chaouki, Microwave heating-assisted catalytic dry reforming of methane to syngas, *Sci. Rep.*, 2018, **8**, 8940.

3 X. Tu and J. C. Whitehead, Plasma-catalytic dry reforming of methane in an atmospheric dielectric barrier discharge: Understanding the synergistic effect at low temperature, *Appl. Catal., B*, 2012, **125**, 439–448.

4 X. Tu and J. C. Whitehead, Plasma-catalytic dry reforming of methane in an atmospheric dielectric barrier discharge: Understanding the synergistic effect at low temperature, *Appl. Catal., B*, 2012, **125**, 439–448.

5 R. Rajagopalan, L. Zhongqi, M. Harigovind, T. Shaon, W. Ruigang and U. Mruthunjaya, Nanoshaped CeO_2 and SiO_2 supported Ru catalyst for plasma catalysis chemical looping reactions, *Int. J. Energy Eng.*, 2020, **10**, 1–12.

6 R. V. Ranganathan, B. Jony, S. M. Fondriest, Z. Liu, R. Wang and M. Uddi, Plasma-catalysis chemical looping CH_4 reforming with water splitting using ceria supported Ni based La-perovskite nano-catalyst, *J. CO2 Util.*, 2019, **32**, 11–20.

7 H. Long, Y. Xu, X. Zhang, S. Hu, S. Shang, Y. Yin and X. Dai, Ni-Co/Mg-Al catalyst derived from hydrotalcite-like compound prepared by plasma for dry reforming of methane, *J. Energy Chem.*, 2013, **22**, 733–739.

8 A. Liu, S. Praserthdam and S. Phatanasri, Investigation on the increased stability of the Ni–Co bi-metallic catalysts for the carbon dioxide reforming of methane, *Catal. Today*, 2020, **358**, 37–44.

9 I. Rossetti, C. Biffi, C. L. Bianchi, V. Nichele, M. Signoretto, F. Menegazzo, E. Finocchio, G. Ramis and A. Di Michele, Ni/SiO_2 and Ni/ZrO_2 catalysts for the steam reforming of ethanol, *Appl. Catal., B*, 2012, **117**, 384–396.

10 G. Zeng, Q. Liu, R. Gu, L. Zhang and Y. Li, Synergy effect of MgO and ZnO in a Ni/Mg–Zn–Al catalyst during ethanol steam reforming for H_2-rich gas production, *Catal. Today*, 2011, **178**, 206–213.

11 C. Crisafulli, S. Scirè, R. Maggiore, S. Minicò and S. Galvagno, CO_2 reforming of methane over Ni–Ru and Ni–Pd bimetallic catalysts, *Catal. Lett.*, 1999, **59**, 21–26.

12 A. A. M. Abahussain, A. S. Al-Fatesh, Y. B. Rajput, A. I. Osman, S. B. Alreshaidan, H. Ahmed, A. H. Fakeeha, A. S. Al-Awadi, R. A. El-Salamony and R. Kumar, Impact of Sr Addition on Zirconia-Alumina-Supported Ni Catalyst for CO_x-Free CH_4 Production *via* CO_2 Methanation, *ACS Omega*, 2024, **9**, 9309–9320.

13 R. A. El-Salamony, A. S. Al-Fatesh, K. Acharya, A. A. M. Abahussain, A. Bagabas, N. S. Kumar, A. A. Ibrahim, W. U. Khan and R. Kumar, Carbon Dioxide Valorization into Methane Using Samarium Oxide-Supported Monometallic and Bimetallic Catalysts, *Catalysts*, 2023, **13**, 113.

14 X. Duan, J. Pan, X. Yang, C. Wan, X. Lin, D. Li and L. Jiang, Nickel–cobalt bimetallic catalysts prepared from hydrotalcite-like compounds for dry reforming of methane, *Int. J. Hydrogen Energy*, 2022, **47**, 24358–24373.

15 S. Zafarnak and M. R. Rahimpour, Co-Ni bimetallic supported on mullite as a promising catalyst for biogas dry reforming toward hydrogen production, *Mol. Catal.*, 2023, **534**, 112803.

16 R. Wang and R. Dangerfield, Seed-mediated synthesis of shape-controlled CeO_2 nanocrystals, *RSC Adv.*, 2014, **4**, 3615–3620.

17 R. Wang, S. I. Mutinda and M. Fang, One-pot hydrothermal synthesis and high temperature thermal stability of $Ce_xZr_{1-x}O_2$ nanocrystals, *RSC Adv.*, 2013, **3**, 19508–19514.

18 Z. Liu, J. Li and R. Wang, CeO_2 nanorods supported M–Co bimetallic oxides (M = Fe, Ni, Cu) for catalytic CO and C_3H_8 oxidation, *J. Colloid Interface Sci.*, 2020, **560**, 91–102.

19 M. R. Ahasan, M. M. Hossain, Z. Barlow, X. Ding and R. Wang, Low-Temperature Plasma-Assisted Catalytic Dry Reforming of Methane over CeO_2 Nanorod-Supported NiO Catalysts in a Dielectric Barrier Discharge Reactor, *ACS Appl. Mater. Interfaces*, 2023, **15**, 44984–44995.

20 R. V. Ranganathan, M. Monir Hossain, S. Talukdar, R. Ahasan, R. Wang and M. Uddi, Tunable Quantum Cascade Laser Absorption Spectroscopy for Plasma Assisted Oxidative Coupling of Methane to C_2 Based Products, *2021 IEEE International Conference on Plasma Science (ICOPS)*, 2021, pp. 1–1.

21 M. M. Hossain, M. R. Ahasan, X. Ding and R. Wang, Coke formation pathway under various reaction conditions during the production of syngas in a dielectric barrier discharge plasma environment using CeO_2 nanorods supported Ni catalysts, *Chem. Eng. J.*, 2024, **479**, 147459.

22 M. Monir Hossain, M. Robayet Ahasan and R. Wang, Influence of catalyst shape on plasma-assisted dry reforming of methane: A comparative study of Ni-CeO_2 nano-cubes and nano-octahedra, *Chem. Eng. J.*, 2024, **496**, 154193.

23 M. R. Ahasan, Y. Wang and R. Wang, In situ DRIFTS and CO-TPD studies of CeO_2 and SiO_2 supported CuO_x catalysts for CO oxidation, *Mol. Catal.*, 2022, **518**, 112085.

24 F. Wang, C. Li, X. Zhang, M. Wei, D. G. Evans and X. Duan, Catalytic behavior of supported Ru nanoparticles on the {1 0 0},{1 1 0}, and {1 1 1} facet of CeO_2, *J. Catal.*, 2015, **329**, 177–186.

25 R. A. El-Salamony, K. Acharya, A. S. Al-Fatesh, A. I. Osman, S. B. Alreshaidan, N. S. Kumar, H. Ahmed and R. Kumar, Enhanced direct methanation of CO_2 using Ni-based

catalysts supported on ZrO_2, CeO_2-ZrO_2, and La_2O_3-ZrO_2: The effect of support material on the reducible NiO-interacted species and catalytic activity, *Mol. Catal.*, 2023, **547**, 113378.

26 T. Jomjaree, P. Sintuya, A. Srifa, W. Koo-amornpattana, S. Kiatphuengporn, S. Assabumrungrat, M. Sudoh, R. Watanabe, C. Fukuhara and S. Ratchahat, Catalytic performance of Ni catalysts supported on CeO_2 with different morphologies for low-temperature CO_2 methanation, *Catal. Today*, 2021, **375**, 234–244.

27 L. Li, B. Jiang, D. Tang, Z. Zheng and C. Zhao, Hydrogen production from chemical looping reforming of ethanol using Ni/CeO_2 nanorod oxygen carrier, *Catalysts*, 2018, **8**, 257.

28 M. Wang, C.-T. Au and S.-Y. Lai, H_2 production from catalytic steam reforming of *n*-propanol over ruthenium and ruthenium-nickel bimetallic catalysts supported on ceria-alumina oxides with different ceria loadings, *Int. J. Hydrogen Energy*, 2015, **40**, 13926–13935.

29 L. Wang, H. Liu, Y. Liu, Y. Chen and S. Yang, Influence of preparation method on performance of Ni-CeO_2 catalysts for reverse water-gas shift reaction, *J. Rare Earths*, 2013, **31**, 559–564.

30 S. Ratchahat, S. Surathitimethakul, A. Thamungkit, P. Mala, M. Sudoh, R. Watanabe, C. Fukuhara, S. S. Chen, K. C.-W. Wu and T. Charinpanitkul, Catalytic performance of Ni/CeO_2 catalysts prepared from different routes for CO_2 methanation, *J. Taiwan Inst. Chem. Eng.*, 2021, **121**, 184–196.

31 Y. Chen, H. Zhang, H. Ma, W. Qian, F. Jin and W. Ying, Direct conversion of syngas to ethanol over Rh–Fe/γ-Al_2O_3 catalyst: Promotion effect of Li, *Catal. Lett.*, 2018, **148**, 691–698.

32 X. Li, M. Wu, Z. Lai and F. He, Studies on nickel-based catalysts for carbon dioxide reforming of methane, *Appl. Catal., A*, 2005, **290**, 81–86.

33 H. Liu, D. Wierzbicki, R. Debek, M. Motak, T. Grzybek, P. Da Costa and M. E. Gálvez, La-promoted Ni-hydrotalcite-derived catalysts for dry reforming of methane at low temperatures, *Fuel*, 2016, **182**, 8–16.

34 T. Sakpal and L. Lefferts, Structure-dependent activity of CeO_2 supported Ru catalysts for CO_2 methanation, *J. Catal.*, 2018, **367**, 171–180.

35 I. Luisetto, S. Tuti, C. Romano, M. Boaro, E. Di Bartolomeo, J. K. Kesavan, S. S. Kumar and K. Selvakumar, Dry reforming of methane over Ni supported on doped CeO_2: New insight on the role of dopants for CO_2 activation, *J. CO2 Util.*, 2019, **30**, 63–78.

36 I. Luisetto, S. Tuti, C. Romano, M. Boaro, E. Di Bartolomeo, J. K. Kesavan, S. S. Kumar and K. Selvakumar, Dry reforming of methane over Ni supported on doped CeO_2: New insight on the role of dopants for CO_2 activation, *J. CO2 Util.*, 2019, **30**, 63–78.

37 M. A. A. Aziz, A. A. Jalil, S. Wongsakulphasatch and D.-V. N. Vo, Understanding the role of surface basic sites of catalysts in CO_2 activation in dry reforming of methane: a short review, *Catal. Sci. Technol.*, 2020, **10**, 35–45.

38 J. Ilsemann, M. M. Murshed, T. M. Gesing, J. Kopyscinski and M. Baeumer, On the support dependency of the CO_2 methanation–decoupling size and support effects, *Catal. Sci. Technol.*, 2021, **11**, 4098–4114.

39 X. Li, D. Li, H. Tian, L. Zeng, Z.-J. Zhao and J. Gong, Dry reforming of methane over Ni/La_2O_3 nanorod catalysts with stabilized Ni nanoparticles, *Appl. Catal., B*, 2017, **202**, 683–694.

40 L. Fan, P. F. Liu, X. Yan, L. Gu, Z. Z. Yang, H. G. Yang, S. Qiu and X. Yao, Atomically isolated nickel species anchored on graphitized carbon for efficient hydrogen evolution electrocatalysis, *Nat. Commun.*, 2016, **7**, 10667.

41 Z. Ma, S. Zhao, X. Pei, X. Xiong and B. Hu, New insights into the support morphology-dependent ammonia synthesis activity of Ru/CeO_2 catalysts, *Catal. Sci. Technol.*, 2017, **7**, 191–199.

42 F. Pan, X. Xiang, Z. Du, E. Sarnello, T. Li and Y. Li, Integrating photocatalysis and thermocatalysis to enable efficient CO_2 reforming of methane on Pt supported CeO_2 with Zn doping and atomic layer deposited MgO overcoating, *Appl. Catal., B*, 2020, **260**, 118189.

43 F. Pan, X. Xiang, W. Deng, H. Zhao, X. Feng and Y. Li, A novel photo-thermochemical approach for enhanced carbon dioxide reforming of methane, *ChemCatChem*, 2018, **10**, 940–945.

44 M. R. Ahasan, M. M. Hossain, X. Ding and R. Wang, Non-equilibrium plasma-assisted dry reforming of methane over shape-controlled CeO_2 supported ruthenium catalysts, *J. Mater. Chem. A*, 2023, **11**, 10993–11009.

45 J. Horlyck, S. Lewis, R. Amal and J. Scott, The impact of La doping on dry reforming Ni-based catalysts loaded on FSP-alumina, *Top. Catal.*, 2018, **61**, 1842–1855.

46 A. Arman, F. Y. Hagos, A. A. Abdullah, R. Mamat, A. R. A. Aziz and C. K. Cheng, Syngas production through steam and CO_2 reforming of methane over Ni-based catalyst-A Review, *IOP Conf. Ser.: Mater. Sci. Eng.*, 2020, 42032.

47 X. Zheng, S. Tan, L. Dong, S. Li and H. Chen, Plasma-assisted catalytic dry reforming of methane: Highly catalytic performance of nickel ferrite nanoparticles embedded in silica, *J. Power Sources*, 2015, **274**, 286–294.

48 D. Ray, P. M. K. Reddy and Ch. Subrahmanyam, Ni-Mn/γ-Al_2O_3 assisted plasma dry reforming of methane, *Catal. Today*, 2018, **309**, 212–218.

49 D. Zambrano, J. Soler, J. Herguido and M. Menéndez, Kinetic study of dry reforming of methane over Ni–Ce/Al_2O_3 catalyst with deactivation, *Top. Catal.*, 2019, **62**, 456–466.

50 M. Khajenoori, M. Rezaei and F. Meshkani, Dry reforming over CeO_2-promoted Ni/MgO nano-catalyst: effect of Ni loading and CH_4/CO_2 molar ratio, *J. Ind. Eng. Chem.*, 2015, **21**, 717–722.

51 Istadi and N. A. S. Amin, Co-generation of synthesis gas and C_{2+} hydrocarbons from methane and carbon dioxide in a hybrid catalytic-plasma reactor: A review, *Fuel*, 2006, **85**, 577–592.

52 X. Tu and J. C. Whitehead, Plasma dry reforming of methane in an atmospheric pressure AC gliding arc discharge: Co-

generation of syngas and carbon nanomaterials, *Int. J. Hydrogen Energy*, 2014, **39**, 9658–9669.

53 P. Chawdhury, K. Bhargavi, M. Selvaraj and C. Subrahmanyam, Promising catalytic activity by non-thermal plasma synthesized SBA-15-supported metal catalysts in one-step plasma-catalytic methane conversion to value-added fuels, *Catal. Sci. Technol.*, 2020, **10**, 5566–5578.

54 N. A. S. Amin, Co-generation of synthesis gas and C_{2+} hydrocarbons from methane and carbon dioxide in a hybrid catalytic-plasma reactor: A review, *Fuel*, 2006, **85**, 577–592.

55 C. Liu, Y. Li, Y. Zhang, Y. Wang, J. Zou, B. Eliasson and B. Xue, Production of acetic acid directly from methane and carbon dioxide using dielectric-barrier discharges, *Chem. Lett.*, 2001, **30**, 1304–1305.

56 N. Lu, X. Bao, N. Jiang, K. Shang, J. Li and Y. Wu, Non-thermal plasma-assisted catalytic dry reforming of methane and carbon dioxide over GC_3N_4-based catalyst, *Top. Catal.*, 2017, **60**, 855–868.

57 M. R. Jahanbakhsh, H. Taghvaei, O. Khalifeh, M. Ghanbari and M. R. Rahimpour, Low-temperature CO_2 splitting in a noncatalytic dielectric-barrier discharge plasma: effect of operational parameters with a new strategy of experimentation, *Energy Fuels*, 2020, **34**, 14321–14332.

58 D. Ray, R. Saha and S. Ch, DBD plasma assisted CO_2 decomposition: influence of diluent gases, *Catalysts*, 2017, **7**, 244.

59 M. Li, Z. Sun and Y. H. Hu, Catalysts for CO_2 reforming of CH_4: a review, *J. Mater. Chem. A*, 2021, **9**, 12495–12520.

60 Z. Lian, S. O. Olanrele, C. Si, M. Yang and B. Li, Critical role of interfacial sites between nickel and CeO_2 support in dry reforming of methane: revisit of reaction mechanism and origin of stability, *J. Phys. Chem. C*, 2020, **124**, 5118–5124.

61 M. Li, Z. Sun and Y. H. Hu, Catalysts for CO_2 reforming of CH_4: A review, *J. Mater. Chem. A*, 2021, **9**, 12495–12520.

62 S. Xu, H. Chen, C. Hardacre and X. Fan, Non-thermal plasma catalysis for CO_2 conversion and catalyst design for the process, *J. Phys. D Appl. Phys.*, 2021, **54**, 233001.

63 M. Li, Z. Sun and Y. H. Hu, Catalysts for CO_2 reforming of CH_4: A review, *J. Mater. Chem. A*, 2021, **9**, 12495–12520.

64 Z. Sheng, H.-H. Kim, S. Yao and T. Nozaki, Plasma-chemical promotion of catalysis for CH_4 dry reforming: unveiling plasma-enabled reaction mechanisms, *Phys. Chem. Chem. Phys.*, 2020, **22**, 19349–19358.

65 A. S. A. S. Omran, DFT Study of Copper-Nickel (111) Catalyst for Methane Dry Reforming, *MS thesis*, Texas A&M University, 2019.

66 P. Navascués, J. Cotrino, A. R. González-Elipe and A. Gómez-Ramírez, Plasma assisted dry reforming of methane: Syngas and hydrocarbons formation mechanisms, *Fuel Process. Technol.*, 2023, **248**, 107827.